NASA TECHNICAL NOTE

NASA TN D-3962

c.1

NASA TN D-3962

BLADE-ELEMENT PERFORMANCE OF TWO-STAGE AXIAL-FLOW PUMP WITH TANDEM-ROW INLET STAGE

by James E. Crouse and Donald M. Sandercock

Lewis Research Center
Cleveland, Ohio

NATIONAL AERONAUTICS AND SPACE ADMINISTRATION • WASHINGTON, D. C. • MAY 1967

BLADE-ELEMENT PERFORMANCE OF TWO-STAGE AXIAL-FLOW PUMP WITH TANDEM-ROW INLET STAGE

By James E. Crouse and Donald M. Sandercock

Lewis Research Center
Cleveland, Ohio

NATIONAL AERONAUTICS AND SPACE ADMINISTRATION

For sale by the Clearinghouse for Federal Scientific and Technical Information
Springfield, Virginia 22151 – CFSTI price $3.00

BLADE-ELEMENT PERFORMANCE OF TWO-STAGE AXIAL-FLOW PUMP WITH TANDEM-ROW INLET STAGE

by James E. Crouse and Donald M. Sandercock

Lewis Research Center

SUMMARY

An inlet stage group for a high-suction-specific-speed, multistage axial-flow pump was tested in water. The first stage was composed of a 3-bladed inducer rotor and a tandem-mounted, 19-bladed transition rotor followed by a stator blade row. The first, or inlet, stage was succeeded by a highly loaded second-stage rotor. Radial surveys of flow conditions were made at the inlet and outlet of each blade row. Flow and performance parameters were computed for a number of blade-element sections.

Blade-element parameters are presented as functions of (1) passage height, to indicate matching problems and radial distributions, (2) incidence angle, to indicate operating range and to compare measured and computed reference values, and (3) pump-inlet net positive suction head, to indicate effects of cavitation on blade-element performance. Overall performance characteristics are also included for reference.

The inducer and transition rotor rows compose the rotating portion for a high head-rise first, or inducer, stage. At design flow, an overall head-rise coefficient of 0.325 was measured at efficiency levels of 0.72, 0.92, and 0.99 across the tip, mean, and hub streamlines, respectively. Some decrease in head rise from the noncavitating level was observed at a suction specific speed of 26 500.

The measured performance indicated that deviation angles from the transition and second-stage rotors were generally larger than the design values, particularly in the blade-tip region. As a result, neither of these two rotating blade rows achieved design energy addition. This was the principal cause for the measured pump head rise falling short of the design level.

INTRODUCTION

The functions of the inducer stage of a high-suction-specific-speed pump are (1) to

accept low pressure fluid from the tank and raise it to the pressure level necessary to keep the downstream rotor-blade row free of cavitation, and (2) to set up the desired radial distribution of velocity diagrams at the inlet to the second-stage rotor. A high inducer head rise, without sacrifice of suction-specific-speed performance, reduces the number of stages required to achieve an overall pump head rise and permits the application of higher levels of loading with cavitation-free flow in the second-stage rotor-blade row.

Radial-bladed, helix-type blade rows have been widely used for inducer stages. High head rise is attained by varying the helical lead angle over the rear portions of the blade. The disadvantages of this approach are that little control of the radial gradients of head-rise and velocity diagrams can be exercised, and the principal diffusion of flow occurs after the blade-surface boundary layer has grown and possibly traversed a cavity collapse region.

The first, or inducer, stage of the two-stage, axial-flow pump, whose performance is reported herein, attempts to overcome these disadvantages by utilizing individual, cambered blade sections and two tandem-mounted rotating blade rows followed by a stator row. The first rotating blade row, the inducer row, resembles the usual inducer in appearance, low level of loading, and long blade chord. The second rotating row, the transition rotor, is similar to an axial-flow rotor row with a large number of higher loaded, short chord blades. The stator downstream of the second rotor row completes the stage. The third rotating element, the second-stage rotor, which completes this inlet group, is an axial-flow rotor whose design parameters are similar to those of loaded stages in a multistage application.

Reference 1 shows the design, overall performance, and blade row midspan head-rise variations as the pump flow is reduced into the unstable, or stall, operating region. In this report, flow and performance parameters computed across a number of selected blade sections, or blade elements, under both noncavitating and cavitating flow conditions are presented. Data at a number of flow rates covering the stable operating range of the pump are also given. Performance of the individual blade elements is averaged to obtain the overall performance values.

APPARATUS AND PROCEDURE

Test Pump

Pump design procedure is discussed in reference 1, and design velocity diagrams, blade-element-performance parameters, and blade-design parameters are summarized in tables I to III. Pump-design inlet-flow conditions were computed from an optimization

TABLE I. - DESIGN VELOCITY DIAGRAMS

Axial station, n, (See fig. 1)	Streamline number	Radius, r, in.	Axial component velocity, V_z, ft/sec	Velocity, V, ft/sec	Flow angle, β, deg	Relative velocity, V', ft/sec	Relative flow angle, β', deg	Blade tangential velocity, U, ft/sec
1	0 (tip)	3.250	16.5	16.5	0	154.4	83.9	153.5
	2	2.964	↓	↓	↓	141.0	83.3	140.0
	4	2.647				126.2	82.5	125.1
	6	2.287				109.3	81.4	108.1
	8	1.859				89.4	79.4	87.8
	10 (hub)	1.296	↓	↓	↓	63.4	75.0	81.2
2a	0 (tip)	3.087	19.0	35.2	57.4	117.7	80.7	145.8
	2	2.844	23.8	37.1	50.1	108.4	77.3	134.3
	4	2.626	26.6	38.8	46.7	99.4	74.5	124.0
	6	2.411	28.3	40.6	45.8	89.4	71.6	113.9
	8	2.189	29.8	42.6	45.7	78.7	67.8	103.4
	10 (hub)	1.954	31.3	45.2	46.3	67.3	62.3	92.3
2b	0 (tip)	3.087	23.8	38.0	51.3	118.6	78.5	145.8
	2	2.890	27.7	39.4	45.4	111.9	75.7	136.5
	4	2.705	30.0	40.7	42.4	104.8	73.3	127.8
	6	2.520	31.4	42.0	41.5	96.5	71.0	119.1
	8	2.329	32.6	43.4	41.3	87.7	68.2	110.1
	10 (hub)	2.130	33.8	45.2	41.6	78.3	64.4	100.7
3	0 (tip)	3.087	19.6	69.4	73.6	81.7	76.1	145.8
	2	2.864	30.3	73.1	65.5	75.2	66.3	135.3
	4	2.700	36.4	76.6	61.6	70.3	58.8	127.5
	6	2.550	39.8	80.0	60.2	64.8	52.1	120.5
	8	2.404	42.5	83.6	59.5	59.4	44.3	118.6
	10 (hub)	2.258	44.9	87.6	59.2	54.8	35.0	106.7
4	0 (tip)	3.087	35.9	42.2	31.8	128.7	73.8	145.8
	2	2.950	34.2	42.8	37.0	114.8	72.9	135.3
	4	2.800	33.0	43.7	40.9	104.3	71.5	127.5
	6	2.635	32.2	45.0	44.2	94.8	70.1	120.5
	8	2.456	31.7	46.6	47.2	85.5	68.3	113.6
	10 (hub)	2.258	31.7	48.9	49.5	76.5	65.5	106.7
5	0 (tip)	3.087	33.1	85.0	67.1	75.2	63.9	145.8
	2	2.940	↓	88.6	68.1	65.7	59.8	138.9
	4	2.785		92.9	69.1	55.7	53.6	131.6
	6	2.622		98.0	70.3	45.8	43.8	123.9
	8	2.447		104.2	71.5	37.1	27.0	115.6
	10 (hub)	2.258	↓	112.0	72.8	33.1	-.5	106.7

TABLE II. - BLADE-ELEMENT DESIGN PARAMETERS

Blade row	Streamline number	Radius, r, in.		Flow coefficient, a_{φ}	Rotor head-rise coefficient, b_{ψ}	Efficiency, η	Diffusion factor, D	Loss coefficient, $\overline{\omega}$	Change in relative flow angle, $\Delta\beta'$, deg
		Inlet	Outlet						
Inducer	0	3.250	3.087	0.108	0.133	0.655	0.2635	0.125	3.2
	2	2.964	2.844	↓	↓	.740	.2622	.100	6.0
	4	2.647	2.626			.809	.2496	.084	8.0
	6	2.287	2.411			.856	.2309	.080	9.8
	8	1.859	2.189			.899	.1871	.080	11.6
	10	1.296	1.954			.940	.0568	.090	12.7
Transition rotor	0	3.087	3.087	0.155	0.227	0.896	0.4171	0.079	2.3
	2	2.890	2.864	.181	↓	.933	.4356	.055	9.4
	4	2.705	2.700	.196		.948	.4423	.049	14.6
	6	2.520	2.550	.205		.956	.4511	.048	19.0
	8	2.329	2.404	.212		.960	.4564	.052	23.8
	10	2.130	2.258	.220		.963	.4498	.060	29.4
Stator	0	3.087	3.087	0.128	-----	-----	0.5884	0.107	41.8
	2	2.864	2.950	.198	-----	-----	.5757	.096	28.5
	4	2.700	2.800	.237	-----	-----	.5681	.088	20.7
	6	2.550	2.635	.259	-----	-----	.5613	.080	16.0
	8	2.404	2.456	.277	-----	-----	.5520	.074	12.3
	10	2.258	2.258	.293	-----	-----	.5403	.067	9.7
Second-stage rotor	0	3.087	3.087	0.216	0.340	0.887	0.5573	0.113	9.9
	2	2.864	2.940	↓	↓	.914	.5692	.082	12.9
	4	2.700	2.785			.933	.6160	.063	17.9
	6	2.550	2.622			.949	.6822	.053	26.3
	8	2.404	2.447			.962	.7532	.051	41.3
	10	2.258	2.258			.972	.7853	.070	66.0

[a]Blade-tip tangential velocity, 153.5 ft/sec.

[b]Blade-tip tangential velocity, 145.8 ft/sec.

TABLE III. - BLADE DESIGN PARAMETERS

[Leading-edge radius r_{le} = trailing-edge radius r_{te} = 0.010 in.]

Blade row	Streamline number	Radius, in.		Incidence angle, i, deg	Deviation angle, δ, deg	Blade solidity, σ	Blade setting angle, γ, deg	Blade camber angle, φ, deg	Blade chord, c, in.	Maximum blade thickness, t_{max}, in.	Angle at entrance of blade row, κ_e, deg	Angle at outlet of blade row, κ_o, deg	Number of blades
		Inlet	Outlet										
Inducer	0	3.250	3.087	3.0	0.8	3.65	----	1.0	----	0.060	80.9	79.9	3
	2	2.964	2.844	3.3	1.5	3.17	----	4.2	----	.066	80.0	75.8	
	4	2.647	2.626	3.6	2.0	2.95	----	6.4	----	.072	78.9	72.5	
	6	2.287	2.411	4.2	2.5	2.82	----	8.1	----	.078	77.2	69.1	
	8	1.859	2.189	5.0	2.9	2.71	----	9.5	----	.084	74.4	64.9	
	10	1.296	1.954	6.9	3.1	2.62	----	8.9	----	.090	68.1	59.2	
Transition rotor	0	3.087	3.087	2.0	0.5	1.47	76.1	0.9	1.50	0.075	----	----	19
	2	2.890	2.864	2.6	3.0	1.58	68.2	9.8	↓	.084	----	----	
	4	2.705	2.700	3.2	4.4	1.68	62.3	15.8	↓	.093	----	----	
	6	2.520	2.550	3.8	5.4	1.79	56.9	20.6	↓	.102	----	----	
	8	2.329	2.404	4.4	6.2	1.92	51.0	25.6	↓	.111	----	----	
	10	2.130	2.258	5.0	6.6	2.07	43.9	31.0	↓	.120	----	----	
Stator	0	3.087	3.087	0	13.6	1.62	45.9	55.4	1.50	0.120	----	----	21
	2	2.864	2.950	↓	9.0	1.73	46.7	37.6	↓	.108	----	----	
	4	2.700	2.800	↓	6.5	1.82	48.0	27.2	↓	.096	----	----	
	6	2.550	2.635	↓	4.9	1.93	49.7	20.8	↓	.084	----	----	
	8	2.404	2.456	↓	3.7	2.06	51.5	15.9	↓	.072	----	----	
	10	2.258	2.258	↓	2.8	2.22	52.9	12.5	↓	.060	----	----	
Second-stage rotor	0	3.087	3.087	0	4.7	1.53	66.5	14.6	1.75	0.070	----	----	17
	2	2.864	2.940	↓	5.4	1.63	63.5	18.3	↓	.084	----	----	
	4	2.700	2.785	↓	6.7	1.73	59.2	24.6	↓	.098	----	----	
	6	2.550	2.622	↓	8.7	1.83	52.5	35.1	↓	.112	----	----	
	8	2.404	2.447	.7	11.0	1.95	41.9	51.6	↓	.126	----	----	
	10	2.258	2.258	4.0	13.0	2.10	24.0	75.0	↓	.140	----	----	

procedure (ref. 1) based on a suction specific speed of 30 000, a hub-tip radius ratio of 0.4, and the assumption of no inlet whirl. The resulting ideal inlet-flow coefficient was

$$\varphi_i = \frac{V_z}{U_t} = 0.108$$

(All symbols are defined in appendix A.) The average axial velocity was doubled across the first two rotating blade rows; half of the increase was accomplished across each rotor row. The flow passage in the meridional plane is shown in figure 1.

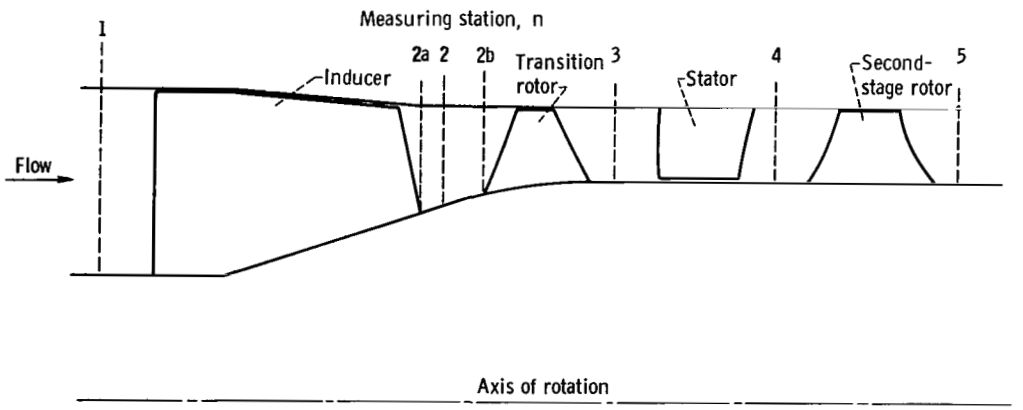

Figure 1. - Meridional view of axial-flow pump.

The first rotating blade row, the second or tandem rotating blade row, and stator blade row, which compose the first stage, will be referred to herein as the inducer, the transition rotor, and the stator row, respectively. The third rotating element, which completes this test unit, will be called the second-stage rotor.

Test Facility

The pump was tested in the Lewis cold-water-pump test facility. Figure 2 shows principal components and the location of each in this closed-loop test facility. Prior to testing, the water was conditioned by routing it through a degasifying system, which decreased the gas content to less than 1 ppm by weight and through a filter capable of removing foreign particles over 5 microns in size. During all portions of the tests, the gas content of the water was maintained below 3 ppm by

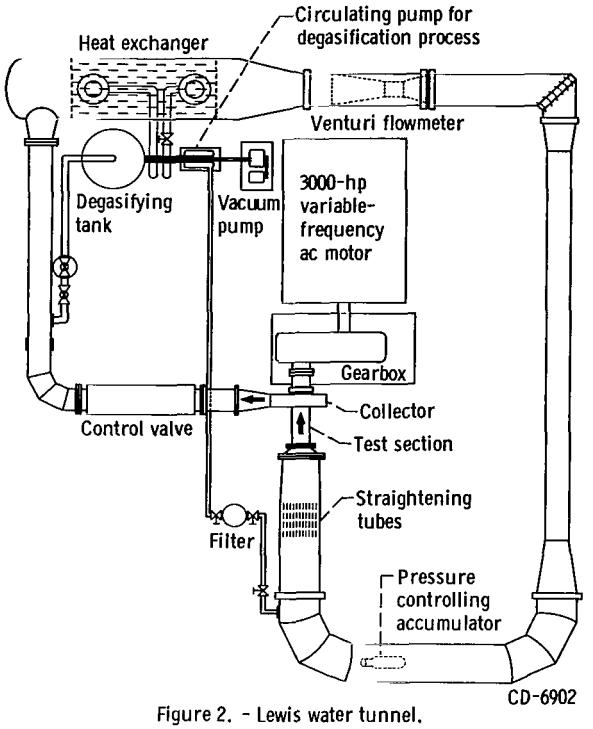

Figure 2. - Lewis water tunnel.

weight. This test facility is discussed more completely in reference 2.

Test Procedure and Instrumentation

The test data used to define the blade row performance presented herein were obtained by operating the pump over a range of flows at constant values of rotative speed and inlet pressure. Characteristic curves were defined for the following conditions: net positive suction head H_{sv} of 246 feet at a rotor tip speed U_t of 123 feet per second; H_{sv}'s of 248, 135, 38, and 15 feet at U_t of 154 feet per second. At each test point, the radial distribution of flow conditions at the inlet and outlet of each blade row (fig. 1) were computed from measurements of total and static head and flow angle taken at five radial positions. These measurement locations were on streamlines bounding approximately 10, 30, 50, 70, and 90 percent of design flow from the tip. The blade elements across a blade row were assumed to lie on the cone that passed through corresponding streamline location points at the inlet and outlet measuring stations.

Instrumentation and control equipment used to measure and set system conditions included a venturi flowmeter, an electronic speed counter used in conjunction with a magnetic pickup, a water temperature recorder and associated automatic control equipment, and a pressure transducer with the associated equipment to measure and main-

tain system pressure automatically. The survey instrumentation included the following items:

(1) Claw probes for measuring total head and flow angle at inducer inlet and behind rotating blade rows (fig. 3(a))

(2) Wedge probes for measuring static head and angle at all measuring stations (fig. 3(b)) (only at the exit of the stator blades, however, were the angle measurements from this type probe used in calculation of performance data)

(3) A 10-tube total head rake for measuring the circumferential variation of total pressure across one stator blade spacing (fig. 3(c))

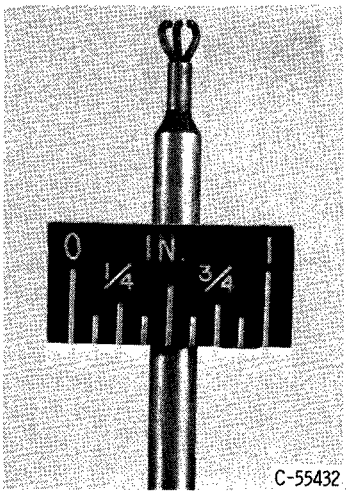

(a) Total pressure claw; tube size, 0.040 inch.

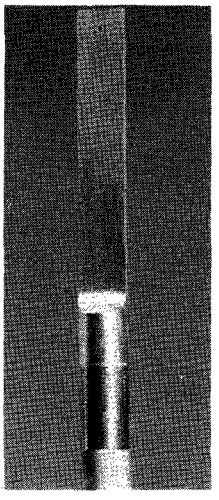

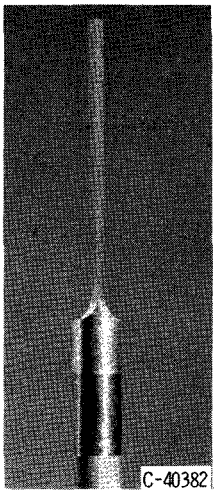

(b) Static pressure wedge; static holes, 0.025 inch.

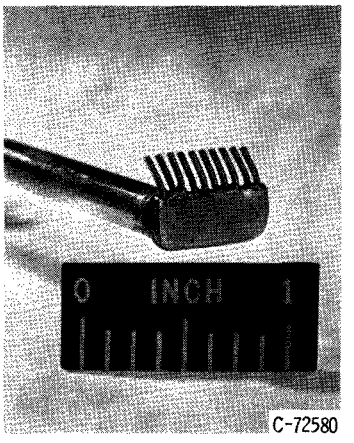

(c) Total pressure wake rake; tube size, 0.035 inch.

Figure 3. - Survey probes.

Each claw and wedge utilized null-balancing, stream-direction-sensitive equipment to aline the probe automatically with the flow direction. A head calibration for each static wedge probe was determined in an air tunnel at approximately the same Reynolds number anticipated during operation in water and applied to the static heads measured in the water tunnel. Pressures were measured with transducers and recorded on paper tape. Inherent accuracies of the measurement and recording devices are estimated to be as follows:

Flow rate, Q_V, percent of design flow	$<\pm 1.0$
Rotative speed, N, percent	± 0.5
Differential heads, ΔH, percent at design flow	± 1.0
Flow angle, β, deg	± 0.5

The accuracy between the single-probe measurements and representative axisymmetric values is also affected by certain indeterminate sources such as circumferential gra-

dients in flow, unsteady flows, cavitation on the probes, etc. These effects could not be evaluated.

Calculation Procedures

The equations used to calculate the blade-element-performance parameters and flow conditions are presented in appendix B. Axisymmetric flow is assumed for all conditions; that is, a single measurement is assumed to represent a reasonable average of flow conditions in the circumferential direction. The test data obtained at station 2 were corrected for area and radius changes to values at stations 2a and 2b (fig. 1, p. 6). Performance and flow parameters across the inducer and transition rotors were computed from values at 2a and 2b, respectively.

Stator-exit average total head was computed by arithmetically averaging the pressures measured from a number of tubes of the rake that most nearly approximated one blade passage at each radial measuring station. At the tip element, for example, a blade spacing required two extra tube spacings. Average total head at this element was obtained by averaging the measurements from the 10 tubes as well as repeating measurements from tubes 1 and 2. At the hub element, tubes 2 to 8 covered a blade spacing. Examples of stator-blade wakes for hub, mean, and tip elements at three different flows covering the range of operation are shown in figure 4. The loss coefficients computed from such pressure measurements vary with both the depth and width of the low-pressure, or wake, areas. These wake parameters are affected by the blade-trailing-edge thickness, the thickness of boundary layers on the blade suction and pressure surfaces, and loss cores occasioned by secondary flows, including blade-tip clearance flows, local scraping of annulus wall boundary layer, radial transport of boundary layer, etc. The examples shown illustrate the summation of these effects on the measured wakes. No attempt is made to isolate the contribution of the various sources.

When the 10-tube rake covered more than a single blade passage, the measurements indicated that the circumferential gradient of pressure in the adjacent passage would be similar, or periodic, except for some operating points in the hub region. For the latter, it is not known if this results from a measurement problem (probe in this location presents a maximum blockage to streamtube flow and is close to inner wall) or a hydrodynamic problem (e.g., tip clearances of adjacent blades may be slightly different and significantly affect secondary flows.

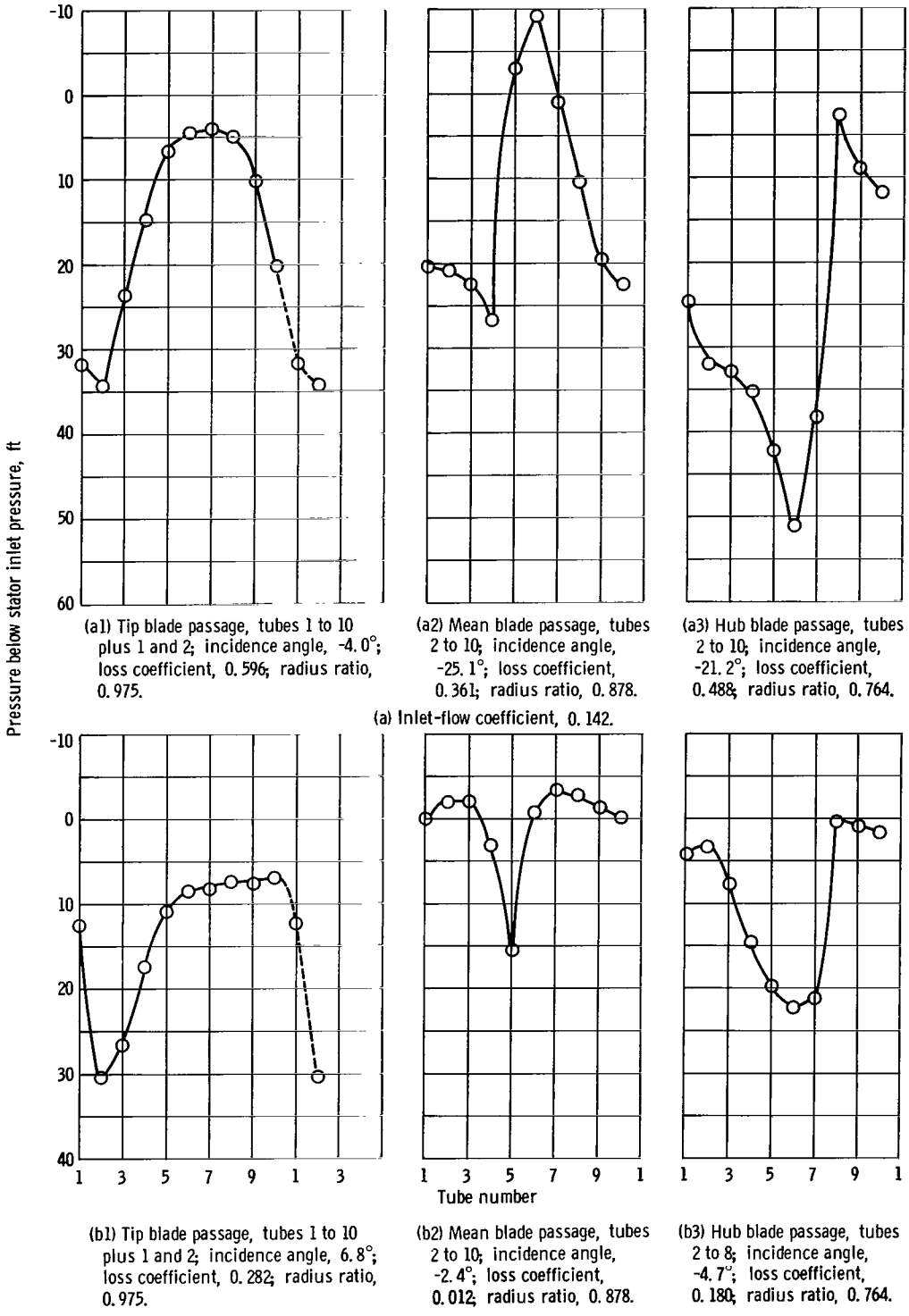

(a1) Tip blade passage, tubes 1 to 10 plus 1 and 2; incidence angle, -4.0°; loss coefficient, 0.596; radius ratio, 0.975.

(a2) Mean blade passage, tubes 2 to 10; incidence angle, -25.1°; loss coefficient, 0.361; radius ratio, 0.878.

(a3) Hub blade passage, tubes 2 to 10; incidence angle, -21.2°; loss coefficient, 0.488; radius ratio, 0.764.

(a) Inlet-flow coefficient, 0.142.

(b1) Tip blade passage, tubes 1 to 10 plus 1 and 2; incidence angle, 6.8°; loss coefficient, 0.282; radius ratio, 0.975.

(b2) Mean blade passage, tubes 2 to 10; incidence angle, -2.4°; loss coefficient, 0.012; radius ratio, 0.878.

(b3) Hub blade passage, tubes 2 to 8; incidence angle, -4.7°; loss coefficient, 0.180; radius ratio, 0.764.

(b) Inlet-flow coefficient, 0.104.

Figure 4. - Examples of stator-blade wakes measured with wake rake (noncavitating).

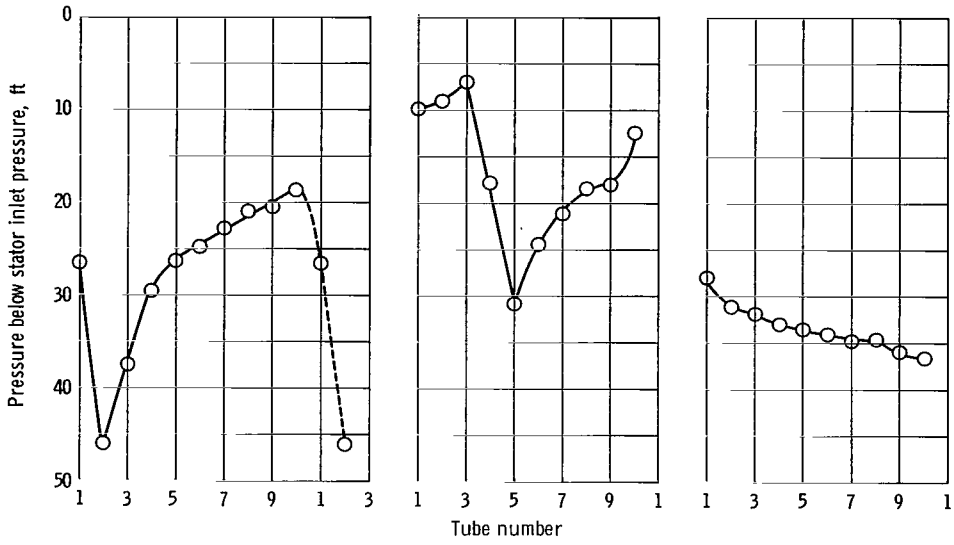

(c1) Tip blade passage, tubes 1 to 10 plus 1 and 2; incidence angle, 12.7°; loss coefficient, 0.379; radius ratio, 0.975.

(c2) Mean blade passage, tubes 2 to 10; incidence angle, 9.3°; loss coefficient, 0.248; radius ratio, 0.878.

(c3) Hub blade passage, tubes 2 to 8; incidence angle, 1.7°; loss coefficient, 0.446; radius ratio, 0.764.

(c) Inlet-flow coefficient, 0.0804.

Figure 4. - Concluded.

Data Reliability

The reliability of the data is determined primarily from a comparison of the integrated weight flow at each measuring station with the weight flow computed from venturi flowmeter measurements. These comparisons are presented in figure 5 in the form $(Q_n - Q_v)/Q_v$ and plotted as a function of $\overline{\varphi}_1$ for quick reference with performance data. The following comments on these flow checks are made:

(1) Under noncavitating conditions (H_{sv} = 246 ft):

(a) At the pump inlet and behind each rotating-blade row, the integrated and venturi flows generally check within ±6 percent. This range is slightly higher than the range generally observed in single-rotor tests.

(b) At the stator outlet (station 4), the flow checks generally show larger discrepancies between integrated and venturi flows; the majority of integrated flows lie in a range of 7 to 15 percent greater than the venturi flows. These relatively large discrepancies probably result from the difficulties in obtaining average values of static pressure and angle behind a stationary-blade row from single measurements. In addition, angle measurements were obtained from a static wedge probe and, in general, are not as accurate as those provided by claw-type probes.

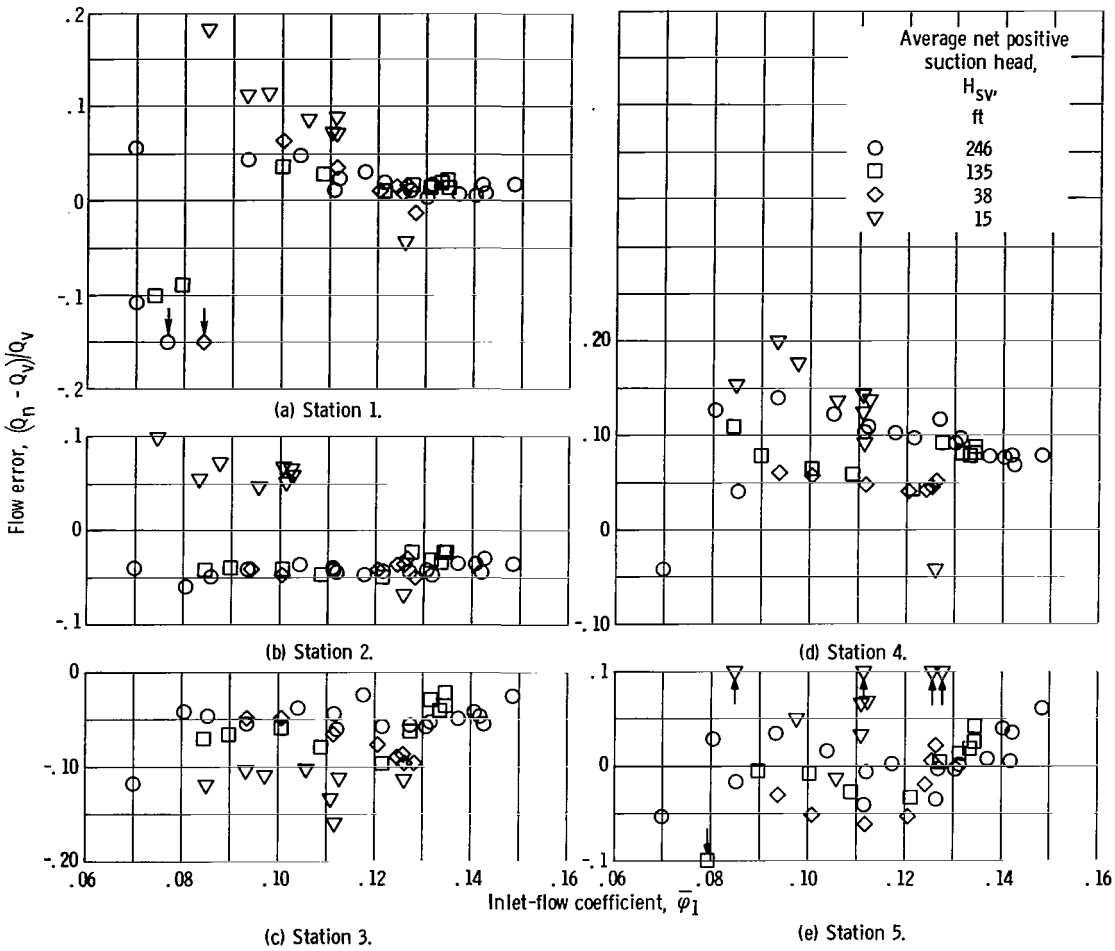

Figure 5. - Comparison of integrated weight flows with those measured on venturi flowmeter.

(2) Under cavitating conditions (H_{SV} = 135, 38, 15 ft): At H_{SV}'s of 135 and 38 feet, the flow checks generally fall within the ranges noted for noncavitating conditions. At an H_{SV} of 15 feet, however, the flow checks show greater discrepancies between integrated and venturi flows over the complete flow range.

General flow conditions that affect the ability to obtain accurate integrated flow values include the following:

(1) As flow is reduced, the accuracy of angle and pressure measurements taken with a measuring system with a given error level becomes more critical with respect to the effect on the computed parameters. For example, a flow-angle error of $\pm 1^{\circ}$ would result in a 1-percent error in V_z (flow) at a flow angle of 30° (typical high-fluid-flow angle) but result in a 3-percent error in V_z at a flow angle of 60° (typical low-fluid-flow angle).

(2) When flow-reversal, or eddy, regions form (as indicated by flow angle meas-

urements of 90° or greater), the reliability of the measurements, particularly static pressures, in and even close to these regions is questionable.

(3) As pump inlet pressures are reduced, cavitation may occur on the probes, particularly affecting static pressure measurements.

RESULTS AND DISCUSSION

The blade-element approach to analysis parallels the blade-element approach to design, as outlined in reference 1. At all flow conditions, fluid streamlines are assumed to lie on the same conical surfaces. Thus, measurements made at given blade-inlet and blade-outlet radii can be related to blade sections, or elements, of known geometry that lie on conical surfaces intersecting the two radial measuring stations. Performance parameters across each blade element are computed and averaged by the methods presented in appendix B. Axisymmetric flow is assumed in all cases. It is recognized that actual flow streamlines will deviate varying amounts from the assumed blade element as flow is varied. The technique just outlined, however, follows that used extensively in compressor research to relate the performance with known blade-element geometry.

Throughout this report, the blade-element flow and performance parameters are not discussed individually but used as necessary to discuss flow conditions at selected operating points. In general, the curves are self-explanatory, and only significant points are discussed.

The noncavitating and cavitating performance are discussed in separate sections. Noncavitating operating flow conditions were based on the premise that, for a given rotative speed, pump overall head rise did not increase as inlet pressure was increased above some bounding value. For this application, a pump-inlet net positive suction head of 246 feet was significantly higher than the bounding value for a blade-tip speed of 123 feet per second and is presented as noncavitating performance. Test facility pressure limitations prevented noncavitating operation over a complete flow range at the design blade speed of 154 feet per second.

Noncavitating Performance

Overall performance. - For reference, the overall performance presented and discussed in reference 1 is shown in figure 6 in which mass-averaged values of head-rise coefficient and efficiency are plotted as functions of an average inlet-flow coefficient. The two branches of the performance curves at the high-flow-coefficient end indicates

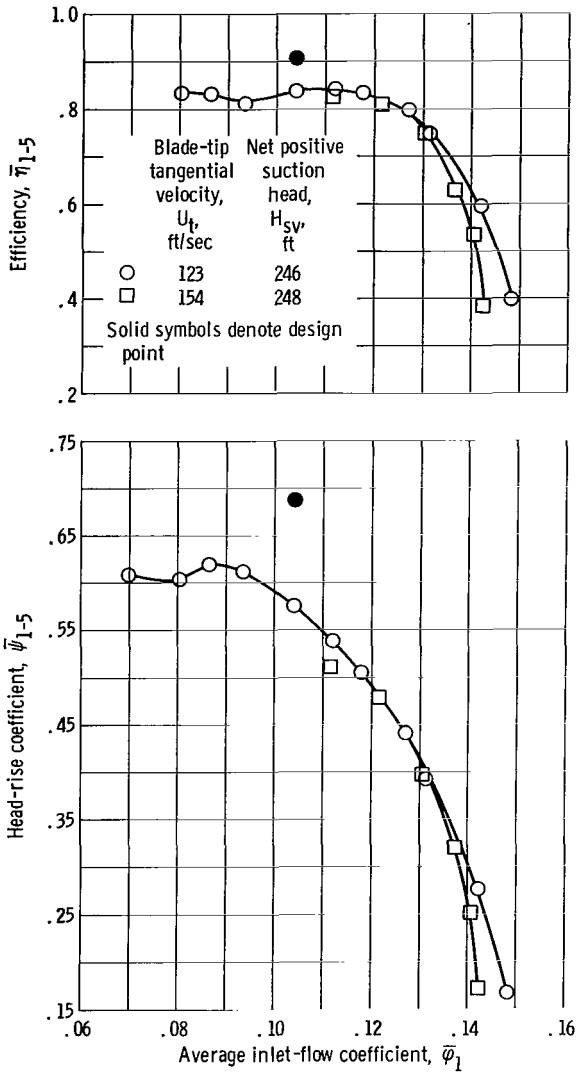

Figure 6. - Overall pump performance for noncavitating conditions.

that, at the higher speed and inlet pressure, cavitation in one or more blade rows of the pump was still affecting performance. The slope of the head-flow-coefficient characteristic is negative from maximum flow (φ_{max} = 0.148) to a flow coefficient of approximately 0.09, at which value it becomes zero or slightly positive. Maximum efficiency of 84 percent occurred at a flow coefficient of approximately 0.112.

For comparison with design, performance at a measured-average-flow coefficient of 0.104 was selected. This assumes a flow blockage caused by hub and tip casing boundary layer at the pump inlet of approximately 4 percent or

$$\varphi = 0.96\ \varphi_i = (0.96)(0.108) = 0.104$$

At design flow, both the measured-head-rise coefficient and efficiency were significantly lower than the design values. The discrepancy between the measured and design efficiencies indicates that measured losses were higher than anticipated at design. In addition, the larger discrepancy between measured and design head rise indicates that the pump did not attain design energy input.

Overall performance of the individual blade rows is indicated in figure 7, which shows the cumulative head rise from the pump inlet to the exit of each blade row and the rotor-blade-row efficiencies. The performance plots in figure 7 show that the inducer attained both design head rise and efficiency, but neither the transition rotor nor the second-stage rotor was able to produce anticipated design levels of performance.

Radial distributions of blade-element parameters at design flow. - Computed blade-element parameters are presented as functions of the percentage of passage height from the hub in figure 8. For comparison with design, blade-element parameters obtained at a measured average pump-inlet-flow coefficient of 0.104 are used.

Inducer: At the inducer inlet (fig. 8(a)), a positive flow angle (in the direction of

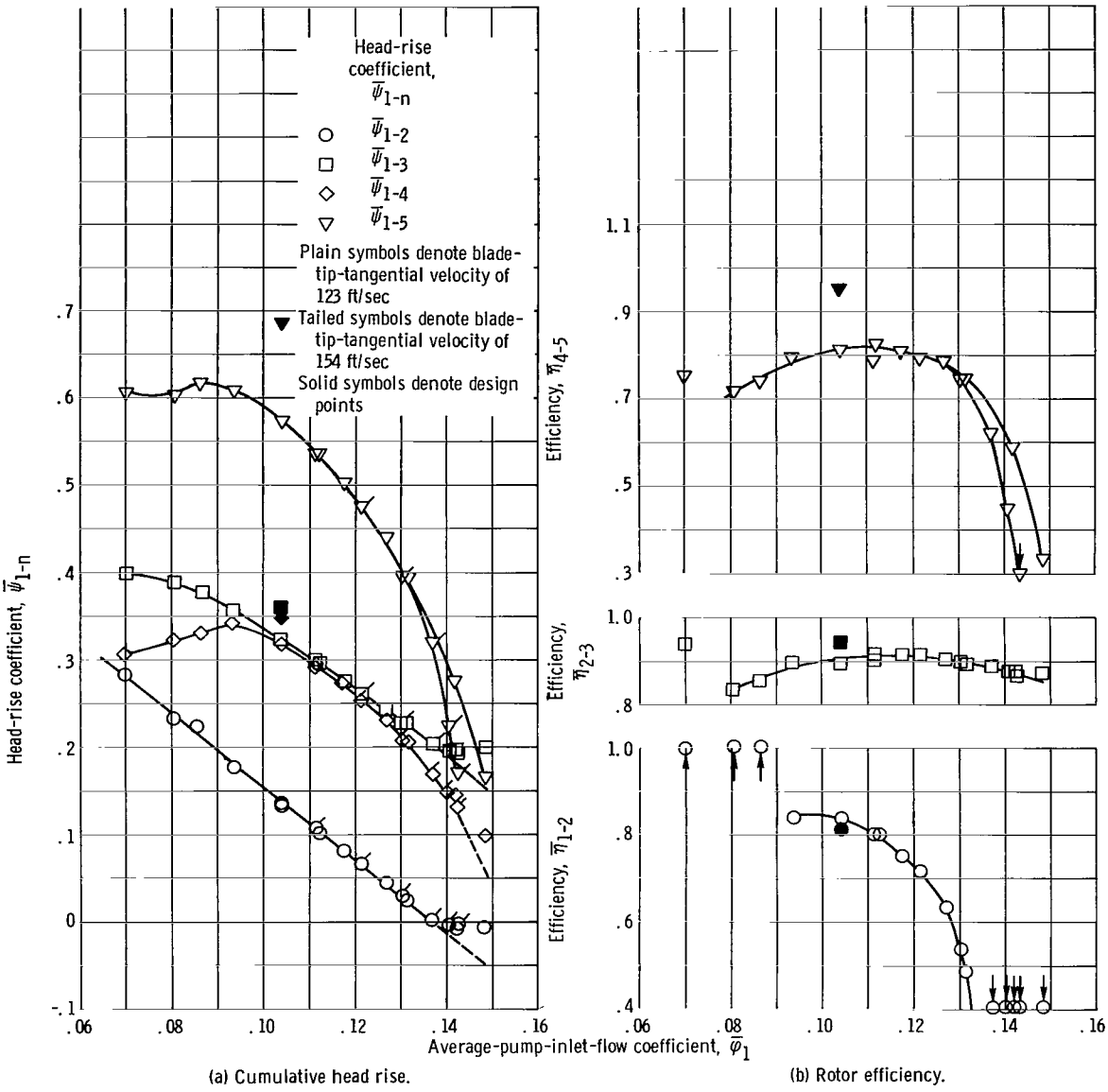

(a) Cumulative head rise. (b) Rotor efficiency.

Figure 7. - Noncavitating performance. Net positive suction head, 246 feet.

rotation) of approximately 13° is measured at the hub element, as compared with the design assumption of no inlet whirl ($\beta_1 = 0$). The measured absolute flow angle in this hub region is probably due to the rotating hub. The effect on the incidence angle at this station is to lower it by approximately 1°.

The radial distribution of measured-loss coefficient for the inducer (fig. 8(b), p. 17) is typical of those observed on other high-solidity, high-blade stagger inducers (refs. 3 to 5). The sharp gradient of loss in the tip regions and the low levels of loss from the mean to the hub region are believed to be indicative of the radial transport of blade

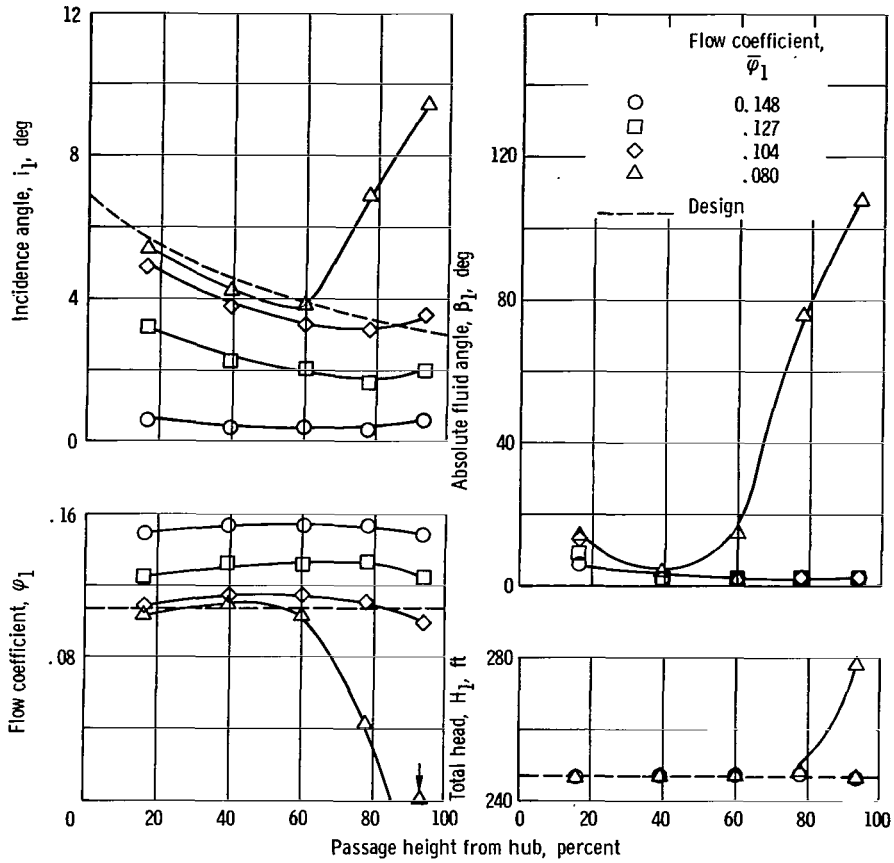

(a) Measuring station 1 (inducer inlet).

Figure 8. - Radial distribution of flow and blade-element-performance parameters. Pump inlet tip speed, 123 feet per second; net positive suction head, 246 feet.

boundary layer and/or other secondary flow patterns.

Measured deviation angles were significantly higher than design at the hub and varied almost linearly across the passage to a value slightly lower than design at the tip. Both the level and radial distribution were similar to those recorded from flat-plate helical inducers (refs. 3 to 5), which indicates that the typical blade-element-design rules for deviation angle are probably not applicable to the high-staggered, high-solidity inducer in which secondary flows apparently have significant effects on flow conditions. The effect of deviation angle on energy input, when combined with that of the loss coefficient, was compensating over most of the passage height, so that the measured-head-rise coefficient did not vary significantly from the design variation except in the tip region.

Transition rotor: The measured performance of the second rotor indicates that neither the transition-rotor-blade deviation angles nor the radial loss gradient (fig. 8(d), p. 19) were anticipated in the design. Measured deviation angles were significantly

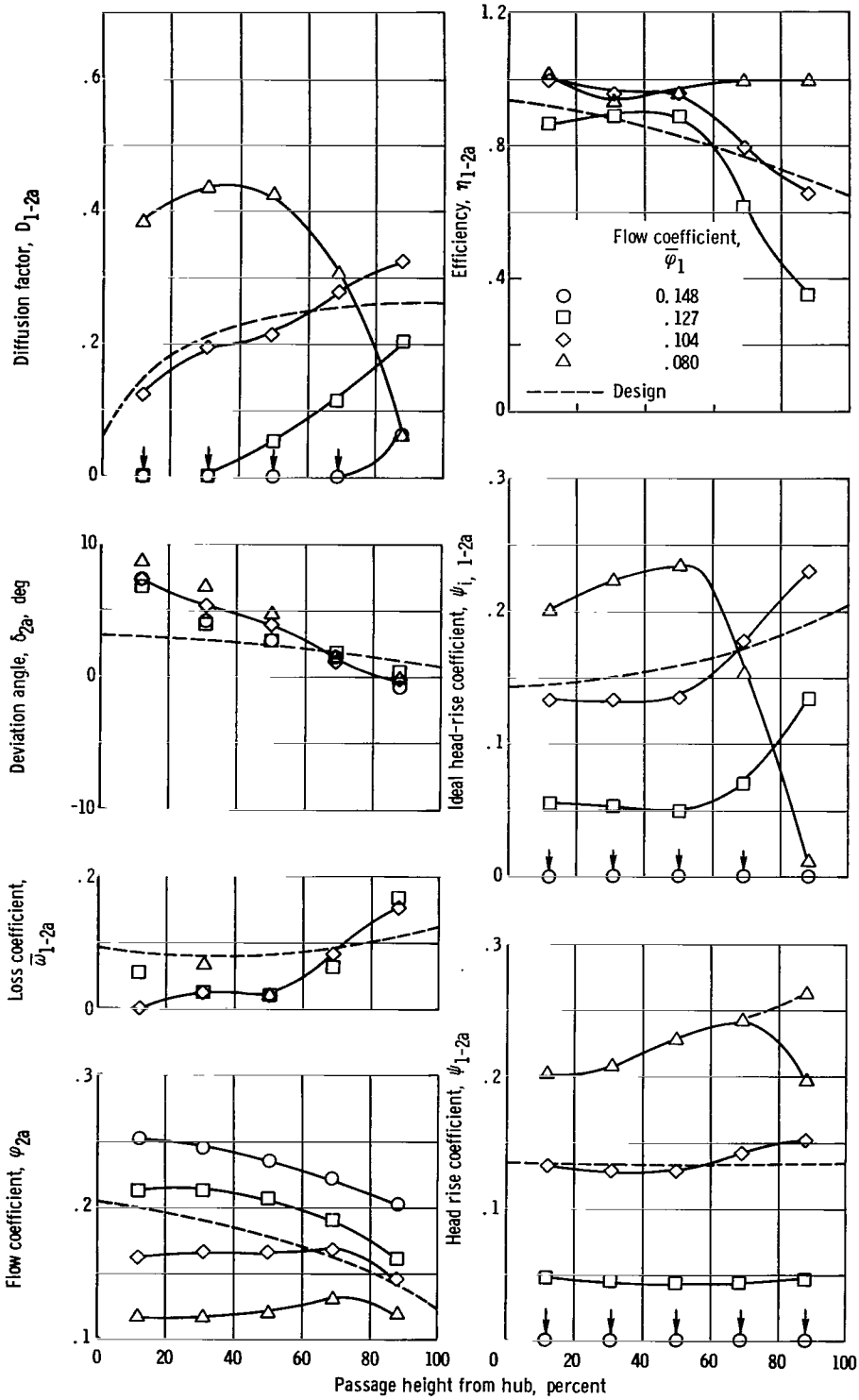

(b) Measuring station 2 (inducer outlet).

Figure 8. - Continued.

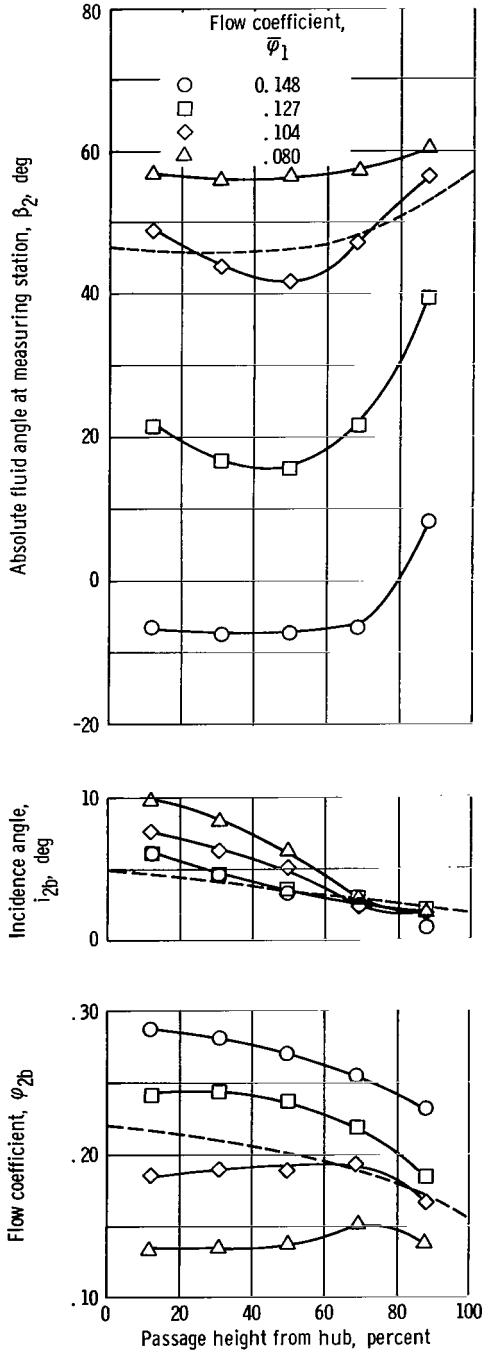

(c) Measuring station 2 (transition rotor inlet).

Figure 8. - Continued.

higher than design at all radii except the hub. One reason for this discrepancy may lie in the design procedure used to predict deviation angles. This design required extrapolation of the method of reference 6 to a range of blade-inlet angles and associated camber angles not covered in the formulation of the rule. In addition, the deviation-angle-prediction method is based on theoretical and experimental investigations of airfoils in cascade, and correction factors or other considerations for additional three-dimensional effects were not applied. Reference 7 discusses qualitatively the effects of secondary flows on the radial distribution of fluid turning (deviation angle).

For any given blade section, the deviation-angle values reflect the level of fluid turning. The higher-than-design levels of measured deviation angle indicate that the desired design fluid turning was not achieved. This, in turn, was the primary reason that design energy addition ψ_i across this rotating blade row was not attained.

The measured-loss coefficients (fig. 8(d)) showed a more severe gradient than anticipated in the design. Measured-loss coefficients were lower than design in the hub region and significantly higher than design in the tip region. This loss distribution, when combined with the radial distribution of energy addition ψ_i, resulted in a lower-than-design head rise at all radii. The plots show that the loss measured at each radii is not always the minimum value measured for that blade element. Thus, all blade sections were not matched for minimum-loss incidence-angle operation at the design flow.

Stator: Across the stator-blade row, the measured-loss coefficients (eq. (B4c) and Calculation Procedure section) were at or below the design values in the blade mean regions but significantly higher in the blade end regions. However, the

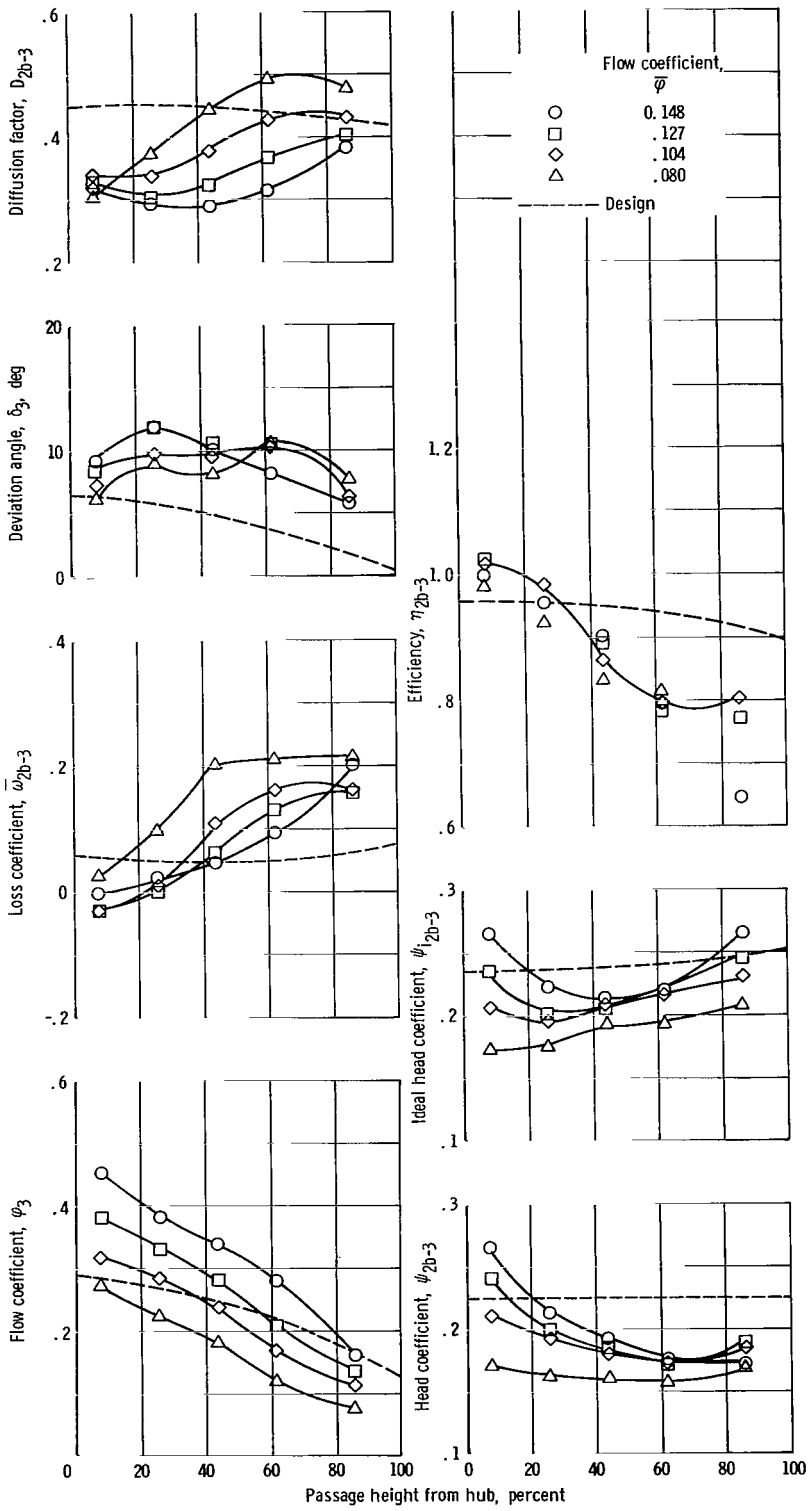

(d) Measuring station 3 (transition rotor outlet).

Figure 8. - Continued.

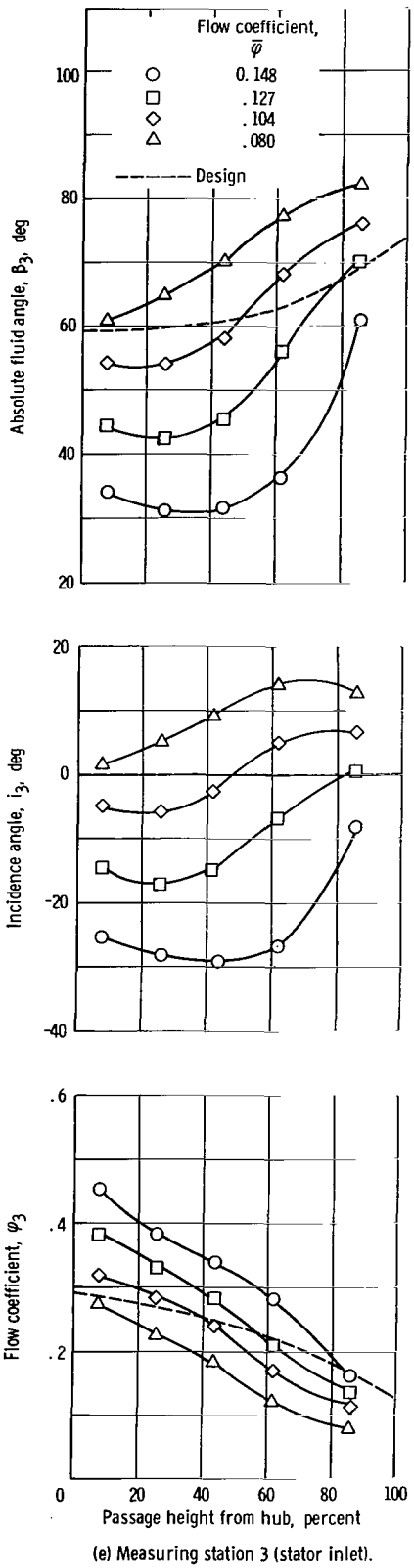

(e) Measuring station 3 (stator inlet).

Figure 8. - Continued.

levels of loss measured at the design flow indicate that the stator blades were operating at or close to minimum-loss incidence angles.

Measured stator deviation angles were lower than design at all radii except in the tip region. It is not clear whether these differences reflect on the design rules or the angle measurements or both. The design procedure to calculate stator deviation angles was the same as that used to compute rotor-blade deviation angles. The differences in the two applications are that the stator-inlet-blade angles are generally slightly lower and the blade element solidities are slightly higher than the angles and solidities of the rotor-blade elements. Again, the design procedure did not apply any considerations for three-dimensional flow effects. It is also believed that the measured stator-outlet-flow angles do not represent as accurate an average value as those measured at the rotor exits (see Test Procedure and Instrumentation section). The negative deviation-angle values seem to support this contention. Higher outlet-flow angles required to provide positive values of deviation angle would also tend to decrease the differences between stator-outlet integrated flows and venturi measured flows (fig. 5, p. 12).

Second-stage rotor: Measured deviation angles at the second-stage rotor exit were significantly higher than design in the blade-tip region (fig. 8(h), p. 23). Likely sources for these differences lie with the design method used, secondary flow effects, and the high loss levels measured throughout the tip regions. The design-blade-inlet angles and associated cambers are outside the range of values compiled in the formulation of the deviation-angle-prediction method (ref. 6), but it seems unlikely that the large discrepancy can be attributed to this fact alone. The prediction of design deviation for this rotor row also did not apply specific considerations for three-dimensional flow effects. Subsequent single-stage pump data (ref. 8) have indicated that, in the blade-tip region, measured three-

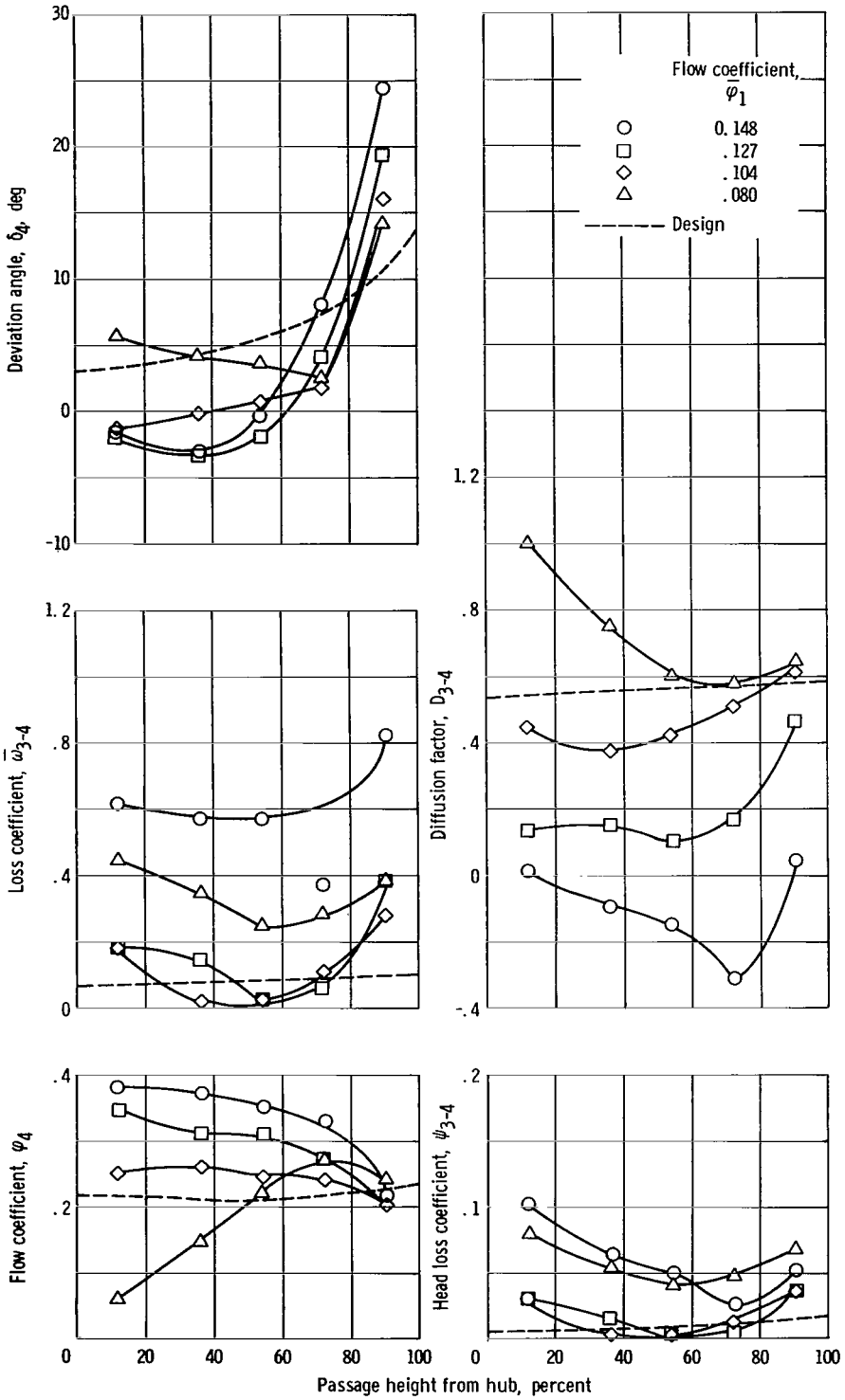

(f) Measuring station 4 (stator outlet).

Figure 8. - Continued.

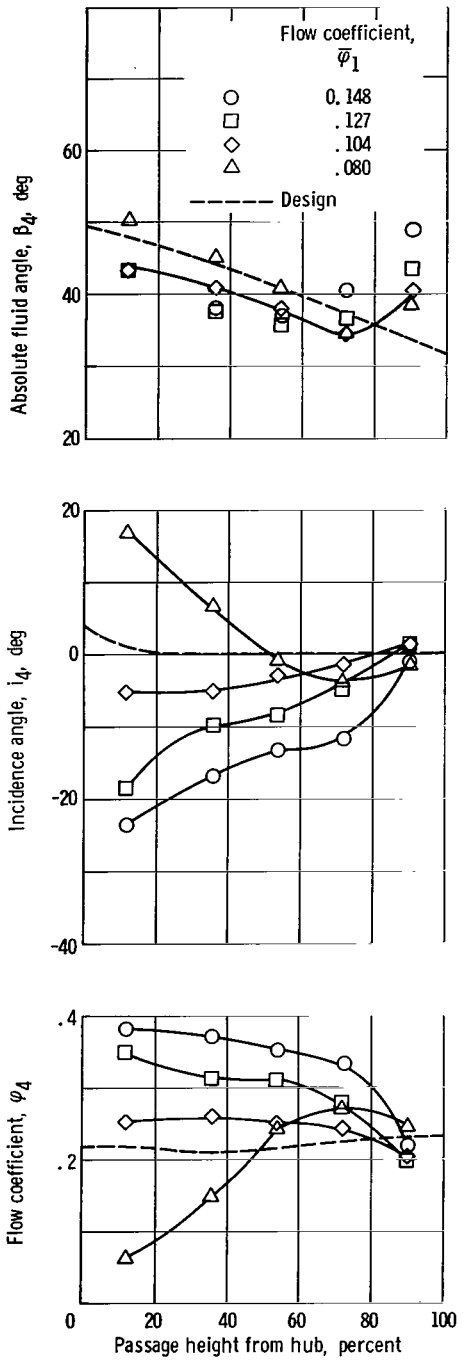

(g) Measuring station 4 (second-stage rotor inlet).

Figure 8. - Continued.

dimensional deviation angles tend to be larger than those calculated for the same blade sections by prediction methods based on two-dimensional cascade data correlations. A further cause for the high level of deviation angle may be the high level of observed loss, both across this particular blade row and the upstream blade rows. In all preceding blade rows, the blade tip section has shown a very high loss, particularly relative to other blade sections. The accumulation of low-energy fluid in this region may be affecting the flow patterns across this rotor row - a stage interaction effect.

Measured-loss coefficients are significantly higher than design at all radii even though at this flow the loss levels are reasonably close to the minimum values measured across each blade element (fig. 8(h)). The latter indicates that the high loss is not caused by operation at an incidence angle significantly different from the minimum-loss value. In the tip region, the high blade loading ($D > 0.6$) offers a cause for the high losses. In the blade mean and hub regions, however, single-stage tests indicate considerably lower loss levels for blade sections operating at close to the same loading (D-factor) levels (ref. 8). The difficulties in obtaining accurate measurements, particularly of static pressure and flow angle, at the stator exit has been discussed in the section Data Reliability. Both these measurements could affect the ideal head-rise calculations (eq. (B1)) across the second-stage rotor which, in turn, are used in loss-coefficient computations (eq. (B4b)). Although it appears likely that the high loss coefficients are in part a result of inaccurate stator-outlet measurements, the extent to which the values are affected at the individual blade elements could not be determined.

The deviation angles and flow coefficients combine such that design energy addition ψ_i is attained at the hub and tip elements, but a lower-than-design

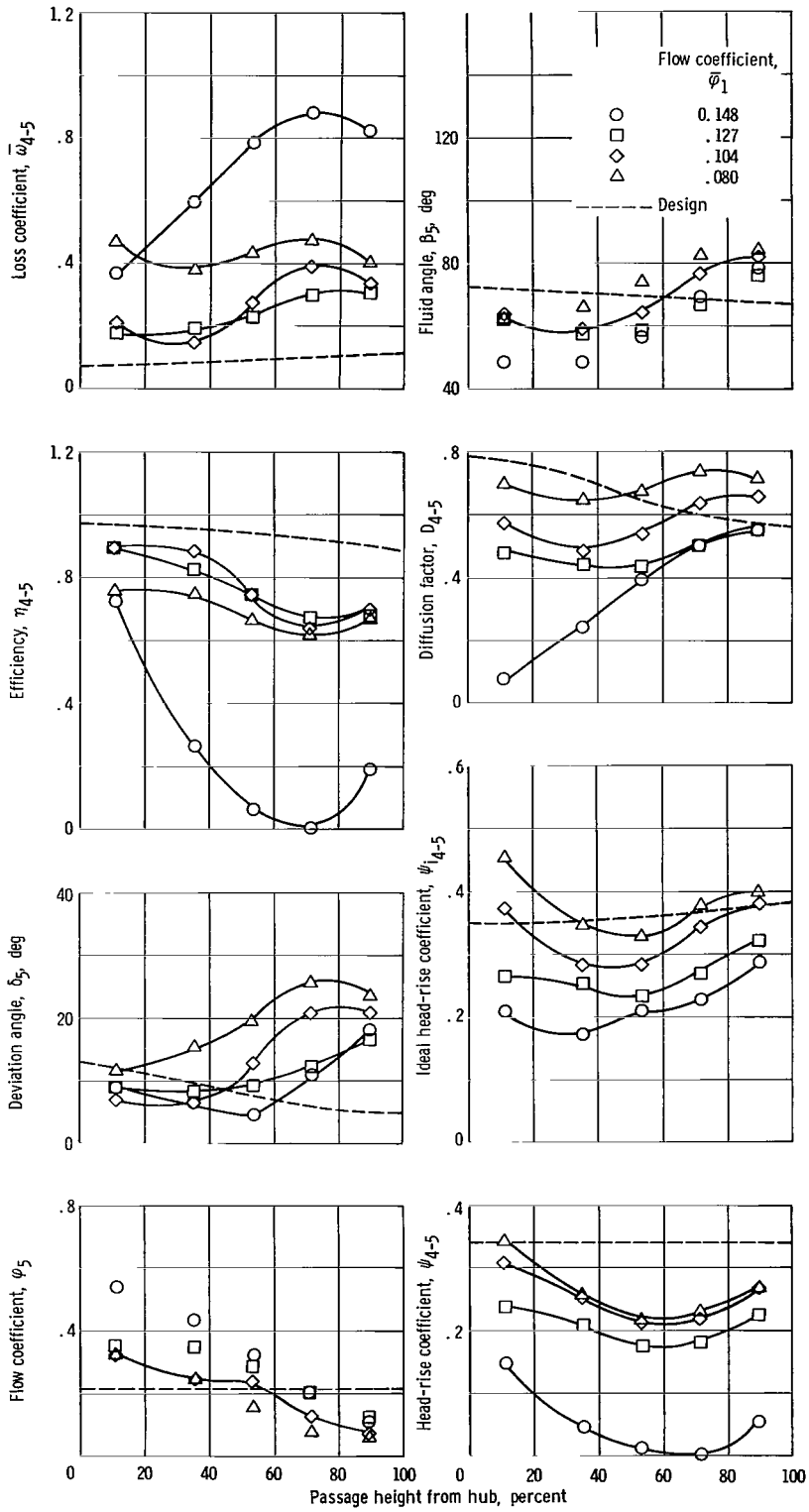

(h) Measuring station 5 (third rotor outlet).

Figure 8. - Concluded.

value is produced at all other elements (fig. 8(h)). This ψ_i distribution and the higher-than-design losses result in below-design values of head-rise coefficient and efficiency at all elements.

In summary, the measured performance at design flow indicates that secondary flows had a significant influence on the radial distribution of loss and possibly deviation angle. All rotating-blade rows showed a rapid increase in loss with radius from the blade mean to tip regions. Differences between measured and design deviation angles were the largest in the blade-tip regions where, in some cases, the blade stagger was sufficiently high to require extrapolation of correlated data from which the design procedure for calculating deviation angle was formulated. This comparison indicated that care should be exercised in applying the design procedures of reference 6 to highly staggered blade rows. A quantitative evaluation of the effects of secondary flows or blade stagger on deviation angle could not be made.

Radial distributions of blade element parameters at off-design operation. - As more difficult missions require some throttling capability of the engine, the off-design performance of the pump assumes increased importance. The blade element performance of each blade row is examined herein at off-design operation for matching problems and individual-blade-row characteristics that tend to limit the usable flow range of the pump. The rotating-blade rows of this axial flow pump all have high-staggered blade sections, which typically experience sharp changes in performance parameters with modest variations in flow.

Inducer: The radial distributions of blade-element performance show that, as inlet-flow coefficient was reduced to a value of 0.08, an eddy region was developed in the tip region of the inducer inlet (fig. 8(a), p. 16). The measured axial velocities drop off severely to zero values, and absolute fluid angles increase rapidly to values of 90° or greater. The inlet total head at the tip element has increased approximately 30 feet over the general level, which indicates that fluid has entered the inducer, has been energized, and has flowed back out to the inlet measuring station. Similar flow patterns at low flows have been observed during investigations of helical inducers (refs. 3 to 5). Thus far, the extent to which radial equilibrium requirements and tip clearance flows affect the formation and extent of the eddy regions has not been resolved. Further decreases in flow resulted in increases in the radial extent of the flow-reversal regions. In this region, velocity diagrams as well as flow and performance parameters (e.g., ψ_i, D, $\overline{\omega}$, and η) calculated from inlet velocity diagrams have little meaning.

The observed dropoff of inducer-head-rise coefficient in the blade-tip region (fig. 8(b), p. 17) is due to the increased inlet total head in this region. A value of head-rise coefficient based on an inlet head of 246 feet is shown by the dotted line. At this reduced flow, a radial gradient of head-rise coefficient increasing toward the tip is produced by the inducer. Such a change in the distribution of head rise is typical of a high

staggered-blade row with radially constant inlet-flow conditions. For a given reduction of inlet-flow coefficient, the energy addition increases more rapidly for the higher staggered-blade sections at the tip than for the lower staggered-blade sections near the hub. This is easily illustrated by typical velocity diagrams at the tip and hub elements.

As flow is increased from design, an operating point is reached at which the inducer produces no head rise ($\overline{\varphi}_1 \sim 0.137$ in fig. 7, p. 15) and, if flow is further reduced, the inducer will turbine. Because of the particular instrumentation utilized, negative head rise could not be measured, and zero values are shown in figure 8(b) (p. 17) for a flow coefficient of 0.148. As indicated in figure 8(b), zero values of head rise were indicated at all radii. The negative fluid-flow angles measured at the inducer outlet (fig. 8(c), p. 18) also indicate that energy was being removed from the fluid.

The approximate useful flow range for this cambered inducer is set by flows at which zero head rise (maximum flow) and the initiation of an eddy flow region (minimum flow, which occurs at $\overline{\varphi}_1 \sim 0.09$) are measured. It should be noted that the formation of the inducer inlet eddy did not trigger noticeable system instabilities. The eddy flow region, however, is considered a potential source for triggering at least local unstable flows and blade forces, and consequently the flow at which it occurs is used as an approximate limit to stable operating range.

Transition rotor: The transition rotor is essentially the rear portion of the complete inducer. It operates at almost a constant incidence angle and turning angle over the complete range of flows subject to variations of deviation angles of the inducer and transition blade rows. Typical velocity diagrams over a range of flows show that, as flow (axial velocity) is increased, more of the change in V_θ (across the inducer and transition rotors) is accomplished in the transition rotor. Hence, the ideal and actual head rise produced by the transition rotor increases with flow. The overall effect is that the characteristic of the combined inducer and transition rotor has a less negative slope than would be realized if the same design overall head rise were accomplished in two individual stages.

Stator: As flow was increased or decreased from the design value, measured losses increased across all blade elements, but the radial distributions were generally similar (fig. 8(f), p. 21). At all flows, losses in the blade hub and tip regions were increased over those measured in the blade mean region.

The radial distributions of outlet-flow coefficient show significant variations with flow and could result in matching problems with the downstream rotor row. The hub region shows a wide change of flow coefficient, which results in high diffusion rates of flow across the stators (fig. 8(f)) and means that the hub elements of the succeeding rotor must operate over a wide range of incidence angle. The radial distributions of stator outlet-flow coefficient generally reflect the radial variations of total head at this station and result from the head rise across the inducer and transition rotors and the

losses through the stator. In this instance, the changes in radial distribution of head rise produced by the two preceding rotor-blade rows are the primary causes for the changes in radial variation of stator outlet-flow coefficient.

The high levels of loss coefficient measured at the high and low flows indicate that all blade sections operated over a complete range from negative to positive stall.

Second-stage rotor: Over the flow range shown, the radial distributions of flow coefficient at the stator exit (second-stage rotor inlet) resulted in the rotor-tip element operating over a narrow range of incidence angle (fig. 8(g), p. 22), while the hub element operated over a large range of incidence angle. In spite of this small incidence-angle operating range in tip region, the losses (fig. 8(h), p. 23) increase very rapidly at incidence angles lower than the minimum-loss value for this highly loaded rotor. At the high flow ($\overline{\varphi}_1 = 0.148$), because of the high loss levels, the second-stage rotor produces a head rise greater than the stator losses only at the hub and tip elements.

The radial distributions of flow coefficient entering the rotor and leaving the rotor indicate significant axial velocity decreases across the tip portion of the blade span and the reverse trend across the hub portion. Over the operating range, the blade-tip region operates over a very small range of incidence angle (relatively constant fluid turning) but with a decrease in axial velocity across the blade row. Thus, the changes in energy addition ψ_i (fig. 8(h)) or ΔV_θ are due primarily to axial velocity changes rather than fluid turning and are relatively small, particularly as flow is reduced from design. The axial velocity decrease, however, keeps the diffusion rate (D-factor in fig. 8(h)) relatively high over the complete operating range. The actual head-rise variation is dependent on the energy addition ψ_i and the loss coefficient $\overline{\omega}$ and shows no increase as flow is reduced below the design value.

In contrast, over the operating range, the blade-hub section operates with a wide range of incidence angle and fluid turning. The change in energy addition ψ_i is because of fluid turning, although the increase in axial velocity, or flow coefficient, across this blade section tends to reduce the amount of ΔV_θ. In this hub region, a wide change in ψ_i occurs over the flow range shown. The increase in flow coefficient across the hub element also tends to reduce the diffusion rate, or D-factor. Again, the actual head-rise ψ variation results from the energy-addition ψ_i and loss-coefficient $\overline{\omega}$ variations.

The high levels of loss coefficient measured at the high and low flows indicate that all blade sections operated over a complete range from negative to positive stall.

The data indicate generally that a diffusion rate, which is affected by an axial velocity decrease (blade-tip element), does not produce as much energy addition as that same value when it results principally from fluid turning (blade-hub element). It is also notable that, as flow to this pump was reduced from design, the head rise produced by the second-stage rotor did not increase over the design flow value. This is

a blade-row-matching problem and is the reason for the decrease in the slope of the overall performance characteristic (fig. 6, p. 14) at flows below the design value.

Blade-element performance. - The performance of the individual blade elements over a range of operating conditions is presented in figure 9 (pp. 28 to 38) as plots of blade-element-performance parameters against incidence angle. Blade elements at the tip, mean, and hub are shown. Information provided by this form of performance curve includes the following:

(1) Selection of reference incidence angles and associated deviation angles

(2) Levels of minimum loss and associated D-factor

(3) Ranges of incidence angle from the reference value to negative and positive stall (stall is generally defined as the operating point where loss coefficient is some multiple of the minimum loss coefficient)

(4) The manner in which various performance parameters change as operation is varied from the reference or design point (this information is needed in off-design analysis procedures)

(5) Comparison of measured design operating conditions with those predicted from current design procedures

Flow across inducer-type blading (high stagger angles, high solidity, and long passage lengths) has not proven amenable to the blade-element concept for analysis. The radial variation of measured loss appears to be more intimately associated with secondary flow patterns, radial transport of blade-surface boundary layer, etc. than with profile-type losses as generally correlated with D-factor. Measured deviation angles in the blade-tip region are generally very low or even negative, even though this is also the region where highest losses are observed. The small deviation angles computed from measurements at the inducer-outlet measuring station (fig. 1, p. 6) may be explained to some extent by the streamline curvature and by the difference in velocity diagrams at the measuring station and at the radial location where the streamline leaves the blade trailing edge (ref. 3). From the blade tip to the blade hub, deviation angles increase in almost a linear manner. Similar distributions of both loss and deviation angle have been observed in the investigations of flat-plate helical inducers (refs. 3 to 5).

When it is considered as an individual rotor row, the tandem-mounted transition rotor operates over a very limited range of incidence angle and is subject primarily to the variation of the inducer deviation angle. In general, the range of incidence angle covered is not sufficient to clearly define minimum-loss incidence angles or operation to negative or positive blade stall.

Both the cambered inducer and the transition rotor were designed across selected blade elements and as individual rotor rows. Hence, the measured performances across blade tip, mean, and hub elements are presented but are not discussed further.

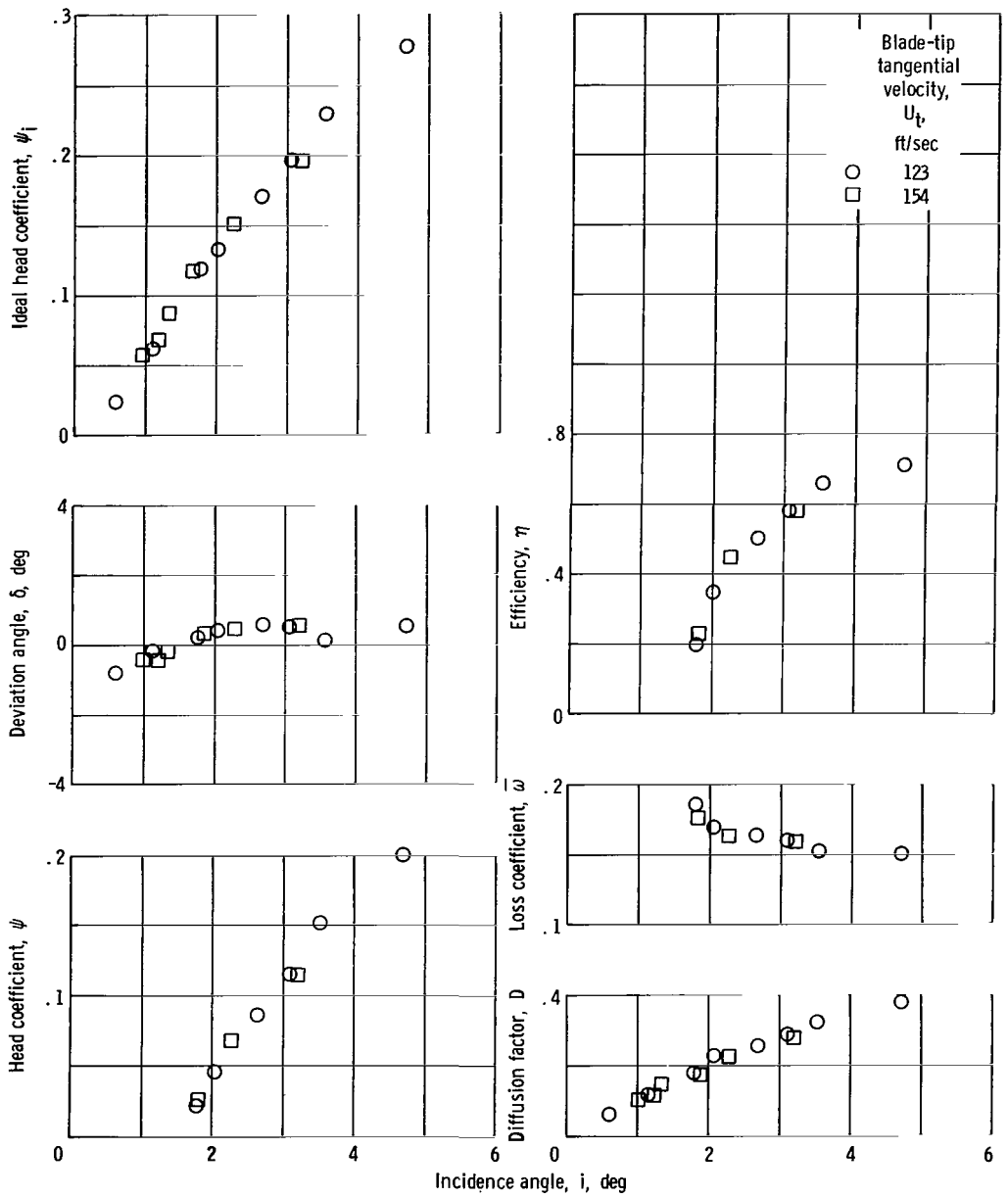

(a) Inducer (near tip); radius ratio, 0.960.

Figure 9. - Blade-element performance (noncavitating). Net positive suction head, 246 feet.

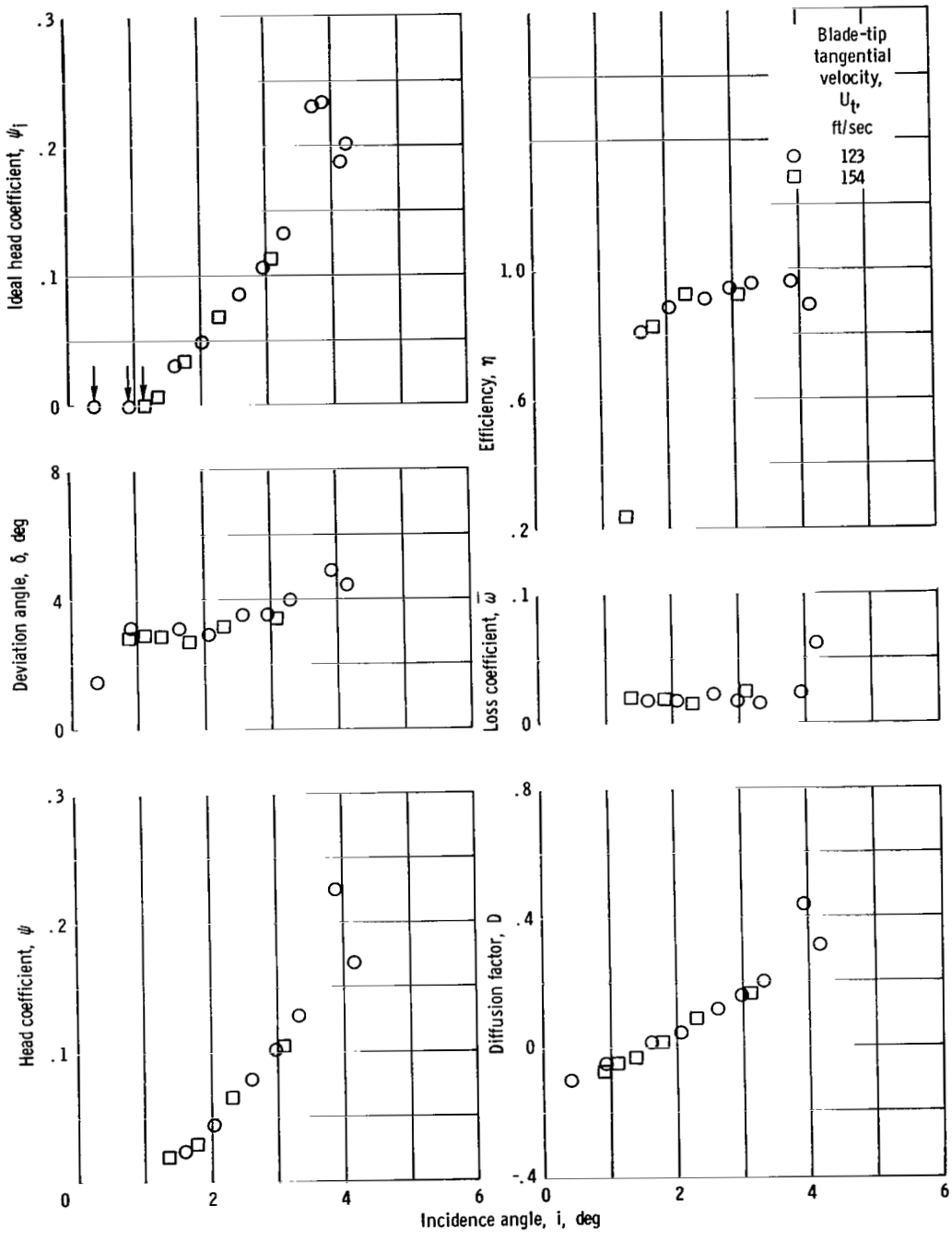

(b) Inducer (mean); radius ratio, 0.813.

Figure 9. - Continued.

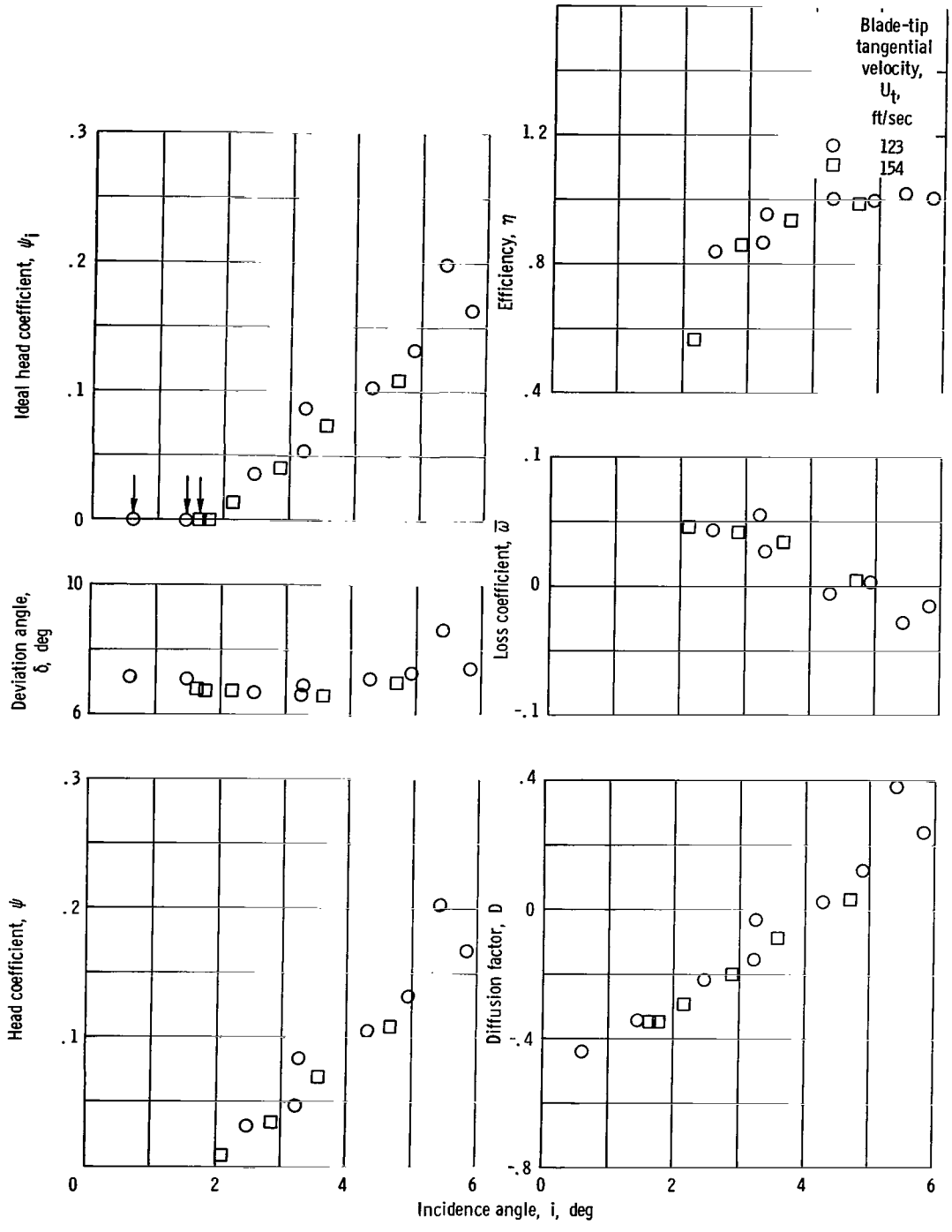

(c) Inducer (near hub); radius ratio, 0.675.

Figure 9. - Continued.

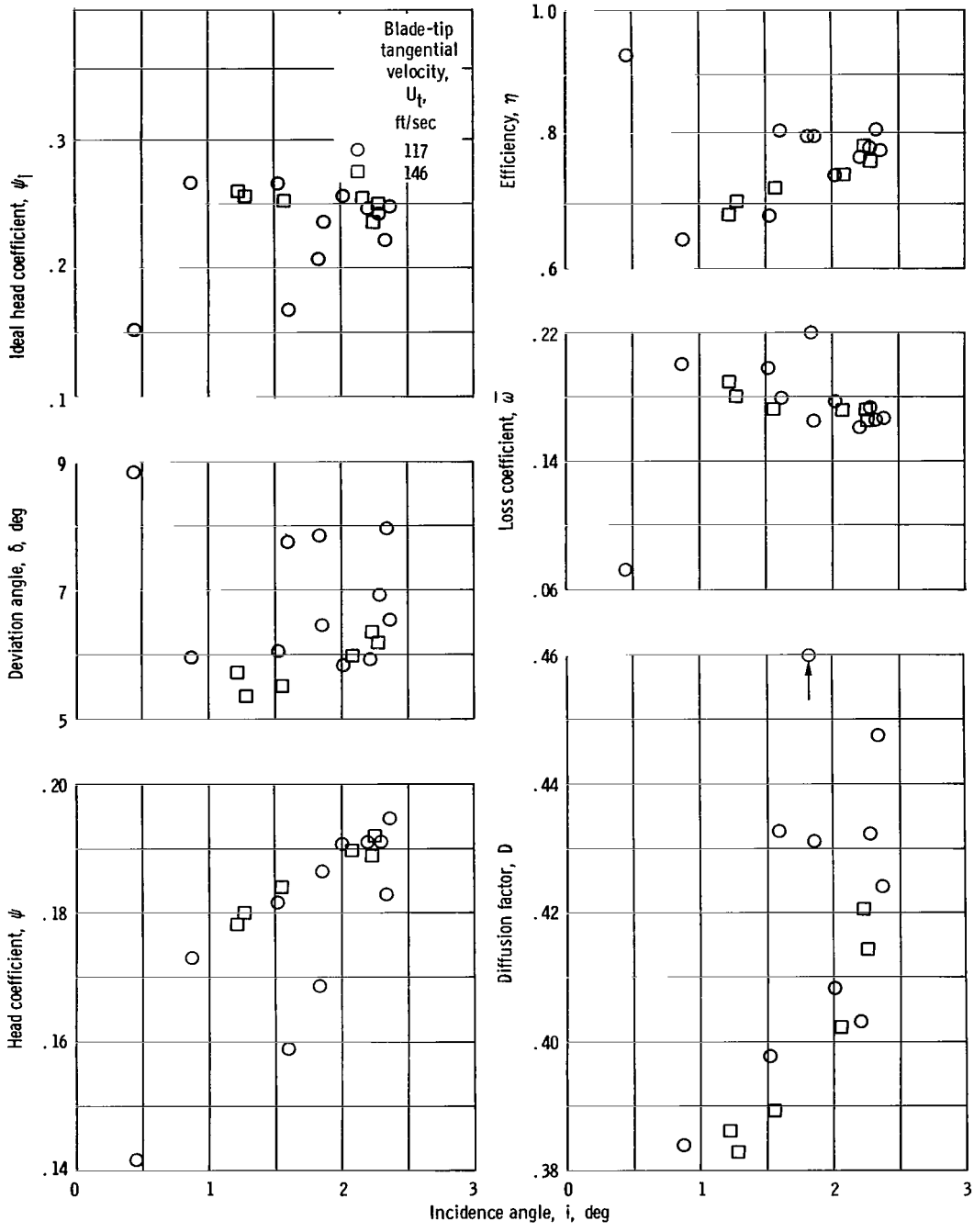

(d) Transition rotor (near tip); radius ratio, 0.962.

Figure 9. - Continued.

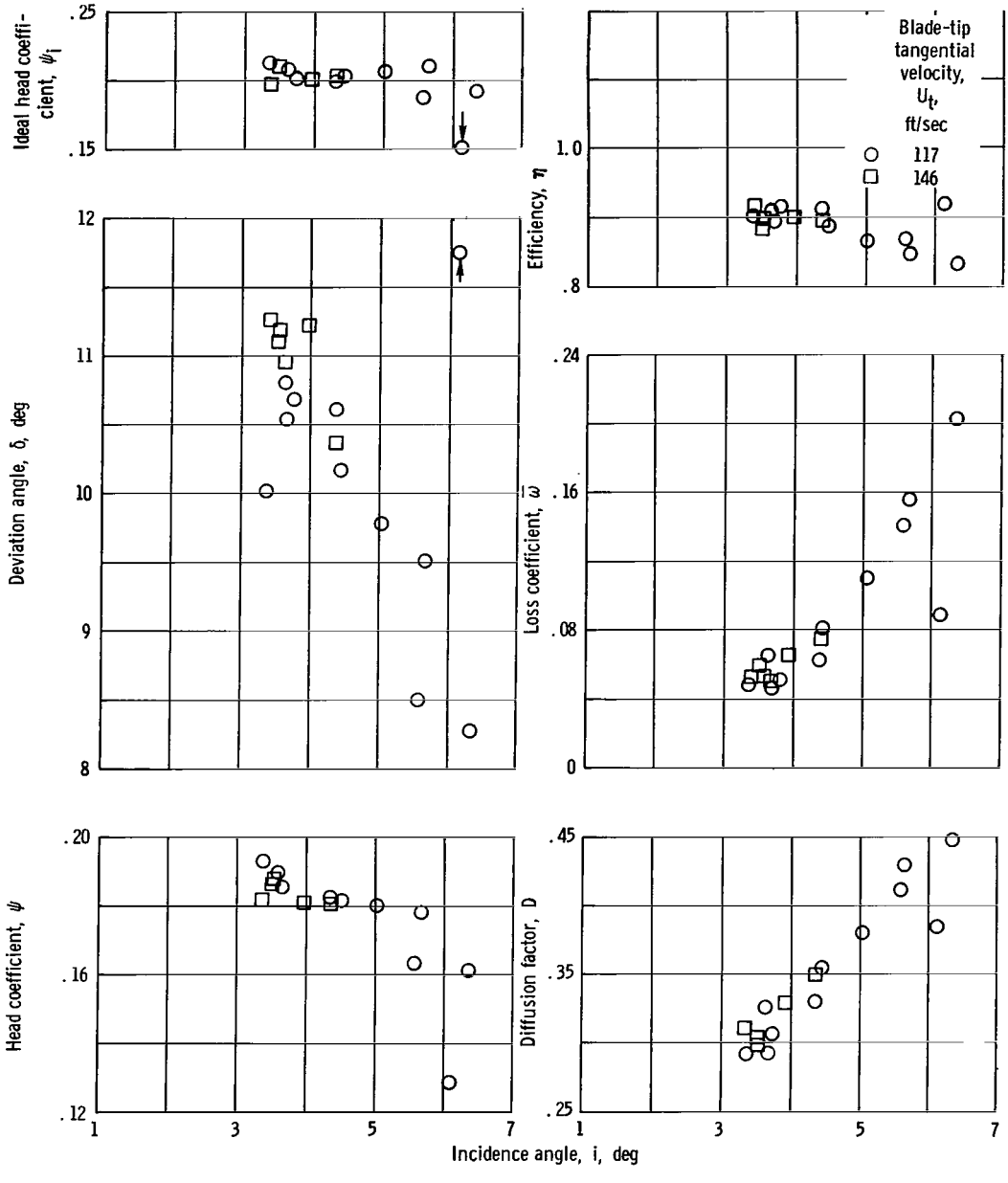

(e) Transition rotor (mean); radius ratio, 0.849.

Figure 9. - Continued.

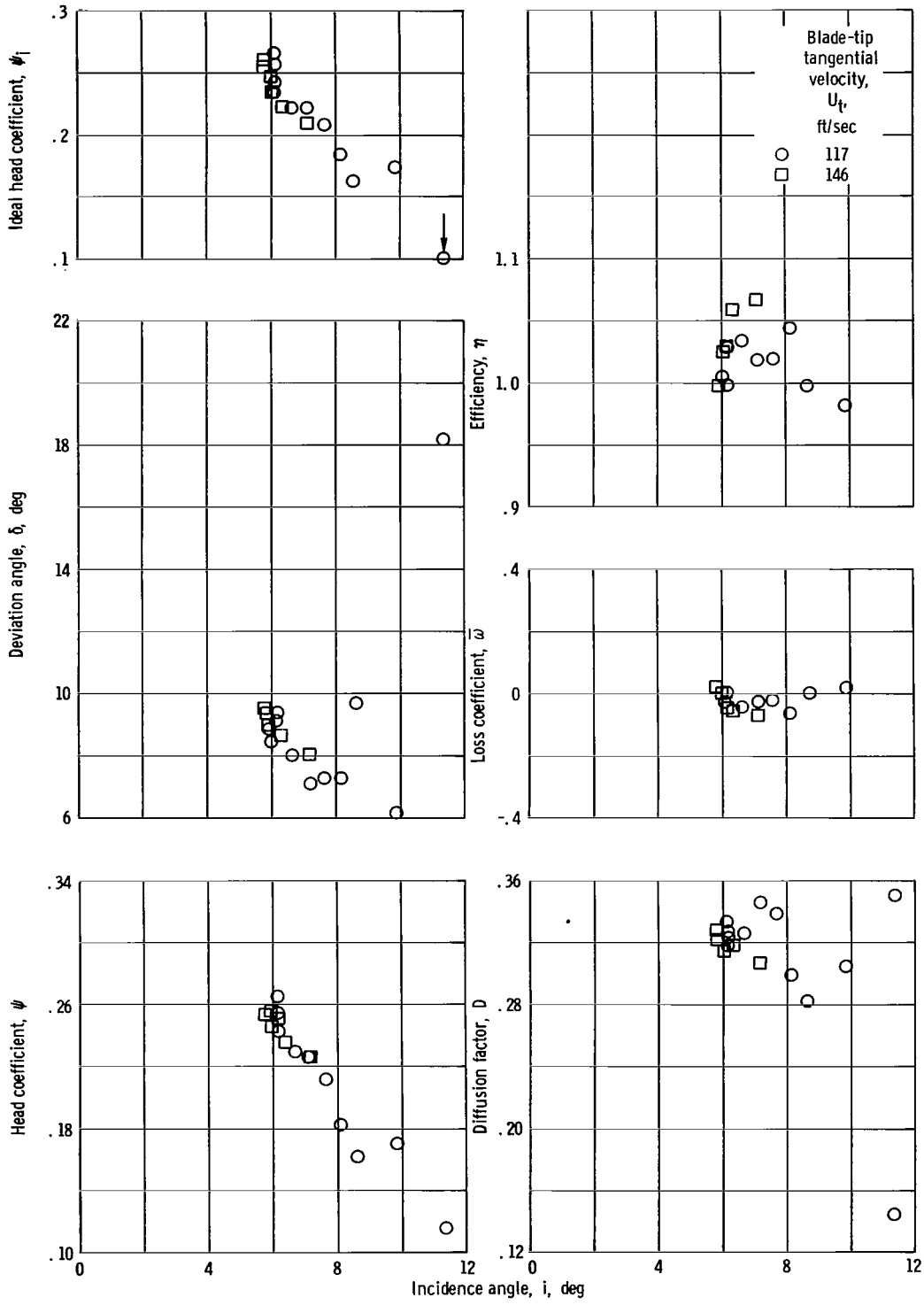

(f) Transition rotor (near hub); radius ratio, 0.752.

Figure 9. - Continued.

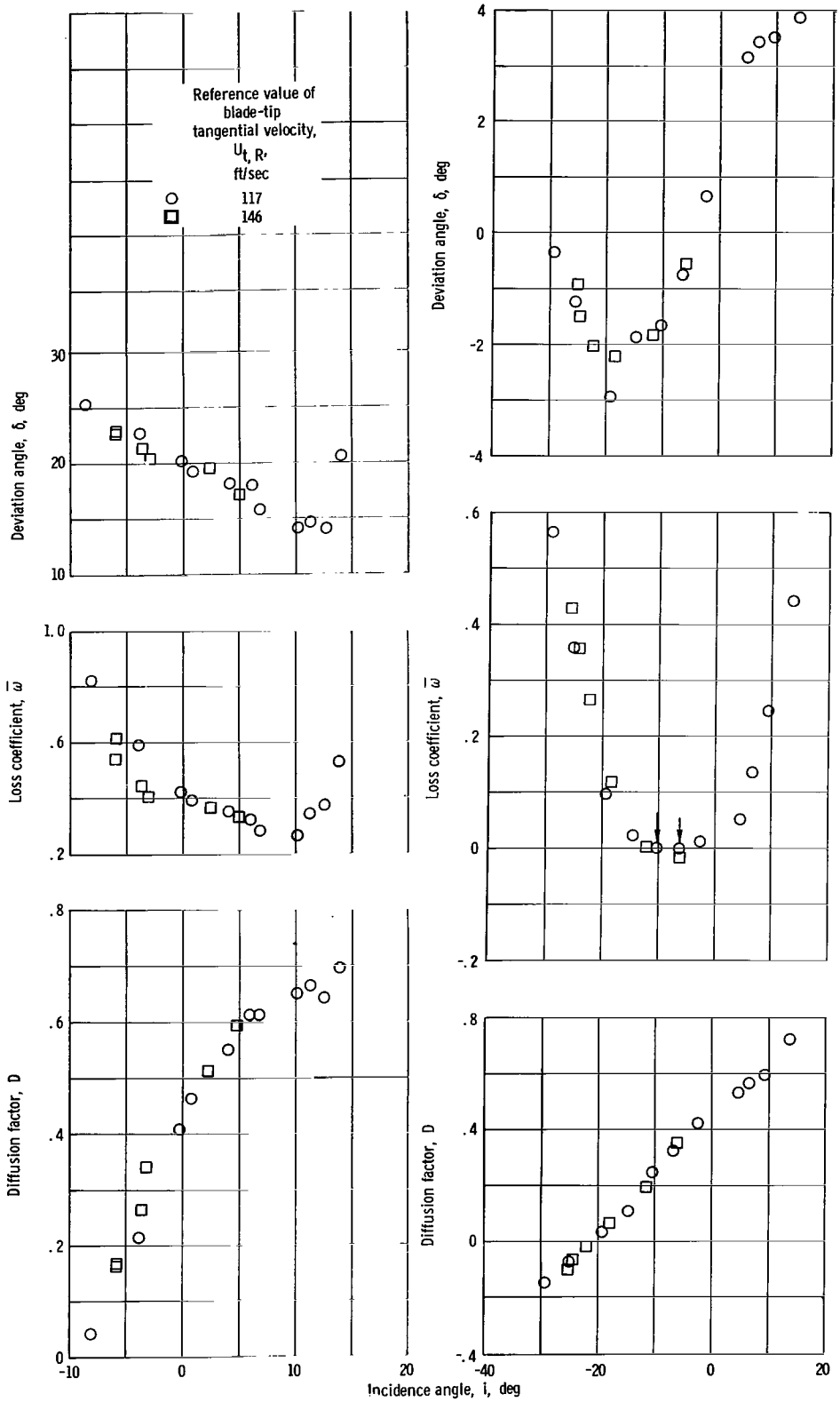

(g) Stator (near tip); radius ratio, 0.975.

(h) Stator (mean); radius ratio, 0.878.

Figure 9. - Continued.

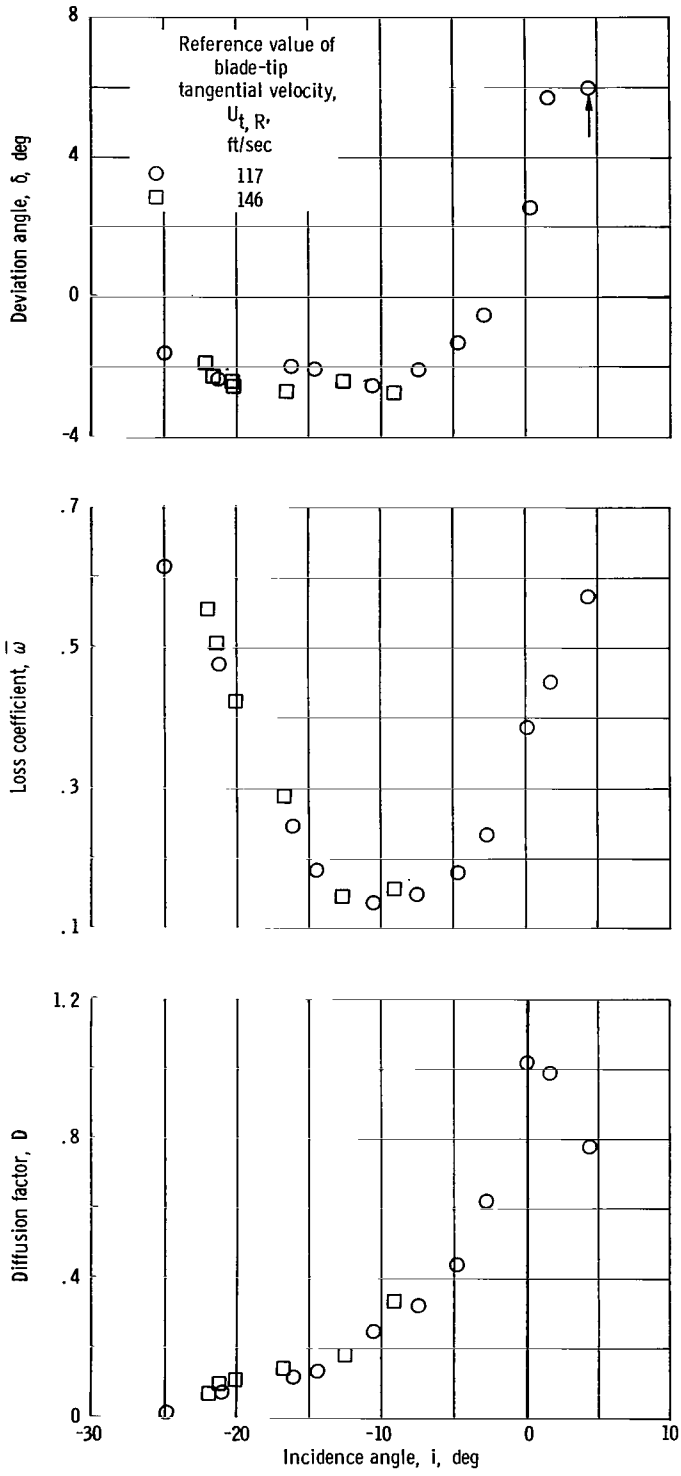

(i) Stator (near hub); radius ratio, 0.764.

Figure 9. - Continued.

The remaining portion of this section discusses the blade-element performance of the stator and second-stage rotor.

Reference values of i, δ, $\overline{\omega}$, and D selected from the plots of figure 9 (pp. 28 to 38) are listed in table IV (p. 39) and are compared with values computed from the design procedures of reference 9. In this summarization, minimum-loss incidence angle is used as the reference incidence angle.

Briefly, the method for calculating reference incidence and deviation angles developed in reference 9 takes the form

$$i_R = i_{2\text{-}D} + (i_R - i_{2\text{-}D})$$

$$\delta_R = \delta_{2\text{-}D} + (\delta_R - \delta_{2\text{-}D})$$

where $i_{2\text{-}D}$ and $\delta_{2\text{-}D}$ are based on empirical correlations of performance of blade sections in two-dimensional cascades, and $(i_R - i_{2\text{-}D})$ and $(\delta_R - \delta_{2\text{-}D})$ are correction factors to account for additional effects on flow about the blade sections when operating in the three-dimensional environment of a pump. In an analysis of the data of table IV and figure 9, the difficulty of obtaining accurate, average measurements of static pressure and angle at the stator exit (see section Data Reliability) should be recollected. This would primarily affect stator-deviation-angle computations and the

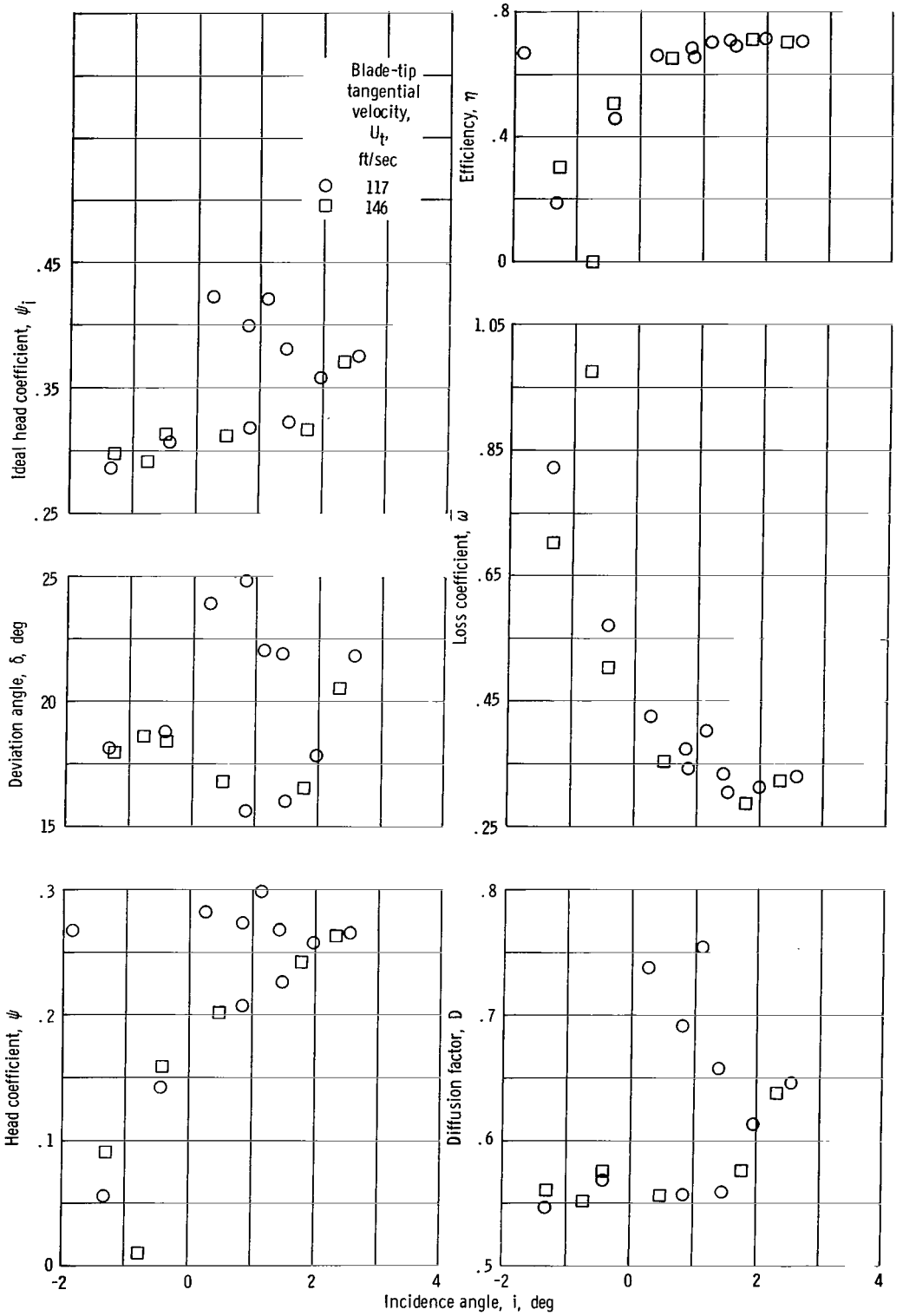

(j) Second-stage rotor (near tip); radius ratio, 0.972.

Figure 9. - Continued.

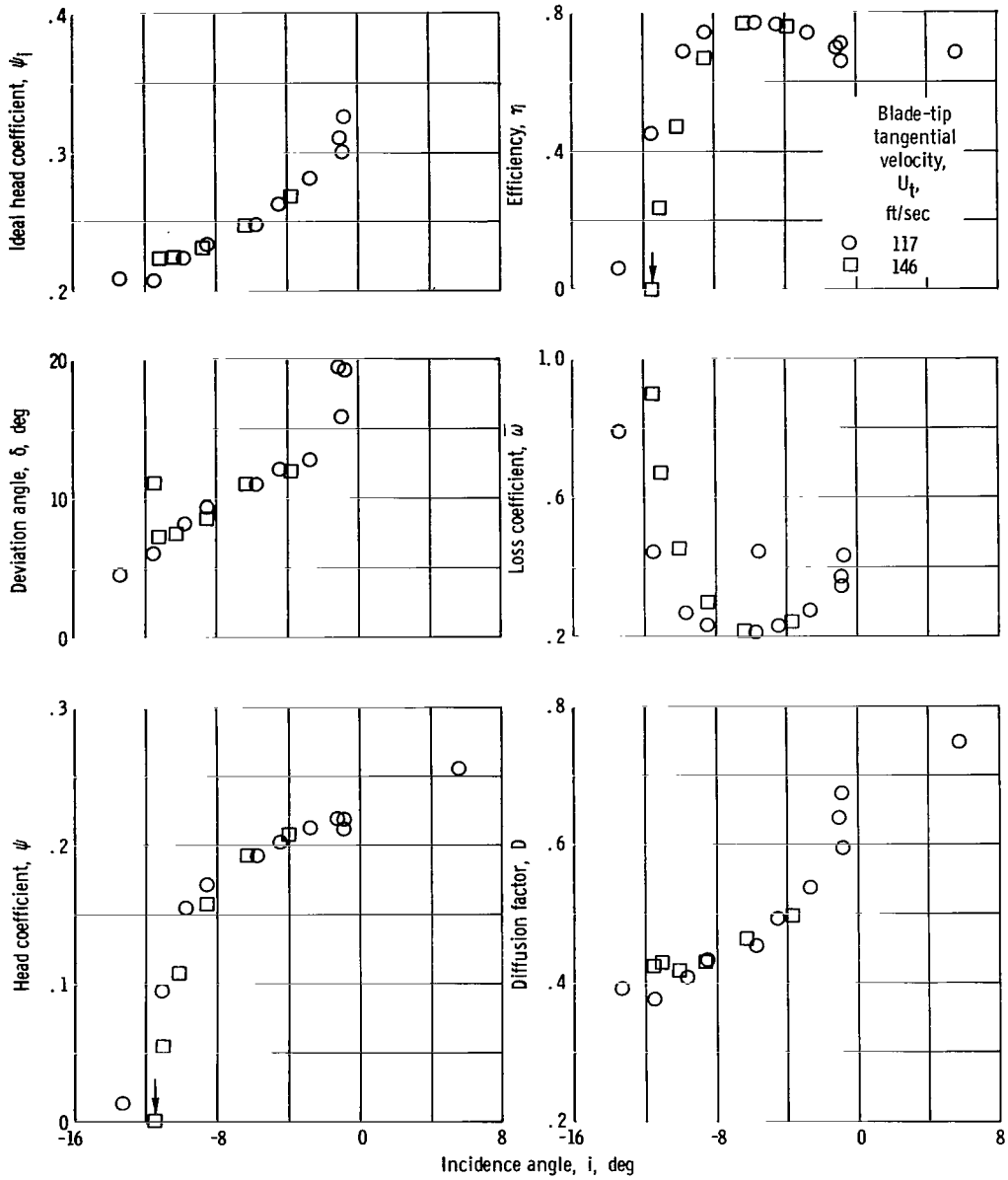

(k) Second-stage rotor (mean); radius ratio, 0.875.

Figure 9. - Continued.

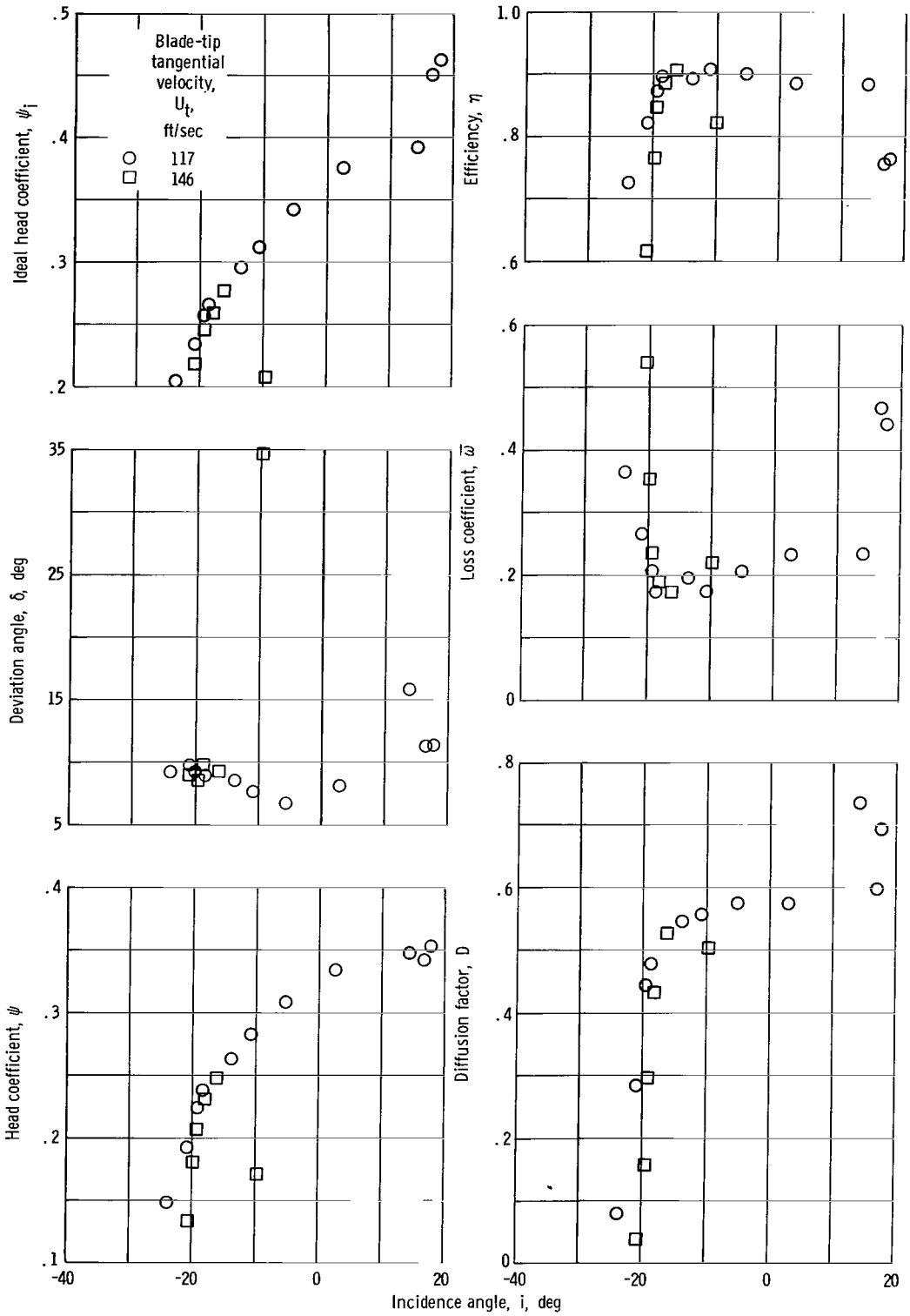

(l) Second-stage rotor (near hub); radius ratio, 0.761.

Figure 9. - Concluded.

TABLE IV. - SUMMARY OF MEASURED BLADE-ELEMENT PARAMETERS AT MINIMUM-LOSS INCIDENCE ANGLE

Blade row	Streamline location	Radius ratio, r/r_t	Minimum-loss incidence angle, i_{ml}, deg	Minimum-loss deviation angle, δ_{ml}, deg	Deviation correction for three-dimensional environment, $\delta_{ml} - \delta_{2\text{-}D}$	Incidence correction for three-dimensional environment, $i_{ml} - i_{2\text{-}D}$	Minimum-loss coefficient, $\overline{\omega}_{ml}$	Total pressure loss parameter at measured incidence angle, $\frac{\overline{\omega} \cos \beta'_o}{2\sigma}$	Diffusion factor, D
Stator	Near tip	0.975	9.5	14.7	1.7	13.8	0.260	0.060	0.65
	Mean	.878	-7.0	----	----	-8.5	0	0	.32
	Near hub	.764	-10.5	----	----	-13.5	.140	.024	.26
Second-stage rotor	Near tip	0.972	1.8	17.0	11.3	2.8	0.290	0.026	0.58
	Mean	.875	-6.0	11.0	-.5	-3.4	.200	.034	.47
	Near hub	.761	-15.0	9.0	-7.0	-9.0	.175	.042	.53

loss levels measured across the second-stage rotor-blade row.

In the tip region of both the stator and the second-stage rotor, the measured minimum-loss incidence angle is positive and higher than that predicted from cascade data, that is, $i_{2\text{-}D}$ values. This probably reflects the effects of tip clearance and secondary flow losses on the determination of the minimum-loss operating point in this region. At all other elements, the measured minimum-loss incidence angles are negative and lower than the computed 2-D values; that is, $(i_R - i_{2\text{-}D})$ is negative. Except for the stator-tip and rotor-hub regions, the variation of loss coefficient with incidence angle is reasonably symmetric about the minimum-loss incidence angle.

A correlation of the measured deviation angles from the second-stage rotor δ_R with $\delta_{2\text{-}D}$ indicates the following:

(1) At the mean radial location, the δ_R closely approximates the calculated $\delta_{2\text{-}D}$ value.

(2) From the mean to the tip, $\delta_R > \delta_{2\text{-}D}$.

(3) From the mean to the hub, $\delta_R < \delta_{2\text{-}D}$.

A correlation with a similar trend was reported in reference 8 for a single-stage axial-flow rotor with double circular arc blades.

Cavitating Performance

Overall performance. - The changes in overall pump performance as inlet pressure is reduced and cavitation occurs in various blade rows of the pump are shown in figure 10. Mass-averaged values of pump-overall-head-rise coefficient and efficiency are plotted as a function of average inlet-flow coefficient (eq. (B11)) and net positive suction

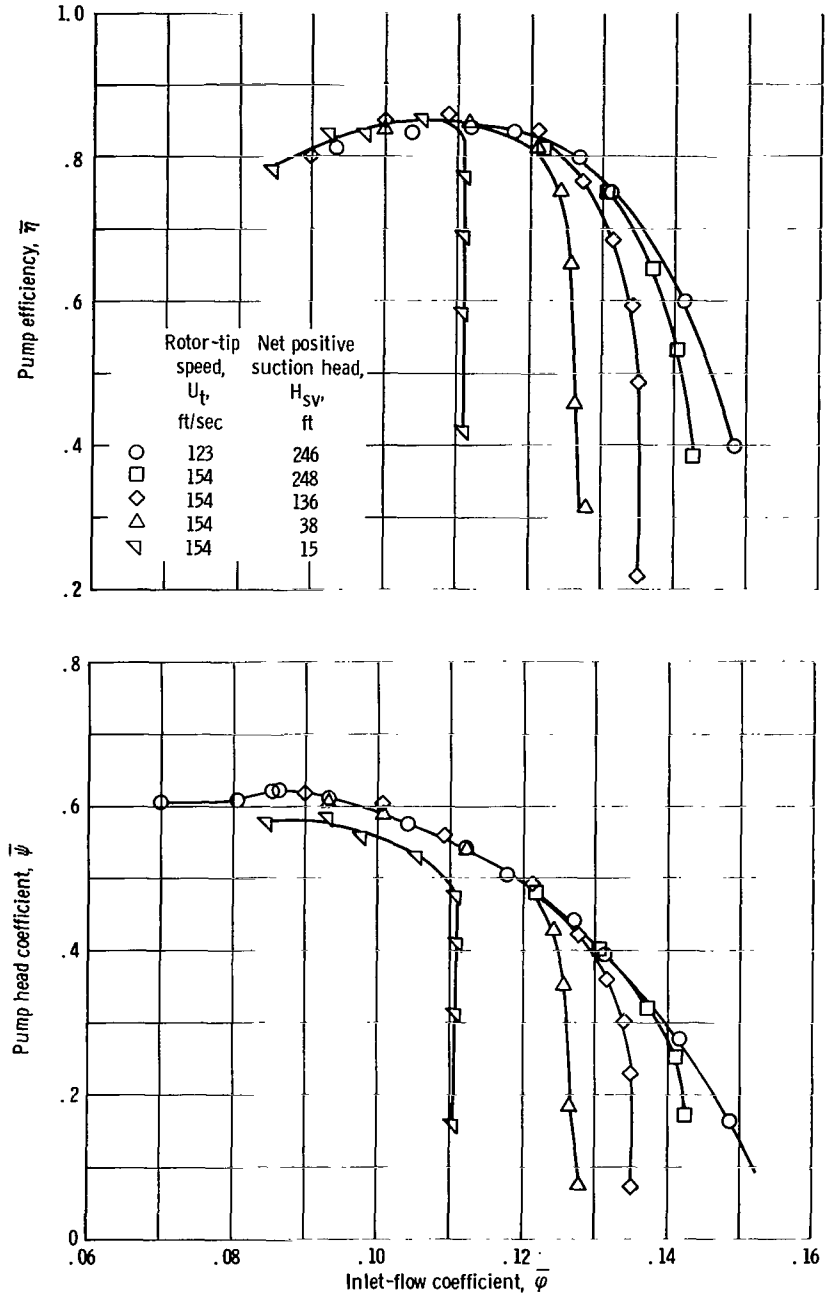

Figure 10. - Overall performance of axial-flow pump under cavitating conditions.

head at the pump inlet. In general, the plots in figure 10 indicate that cavitation results in a reduction of the head-producing capability of the pump, a reduction in the efficiency of the flow processes across the pump, and a reduction in the maximum flow the pump can pass. At a tip speed of 154 feet per second and a net positive suction head of 248 feet, pump performance is affected at flow coefficients above 0.137, which represents a pump suction specific speed of approximately 3700. At design-flow coefficient ($\varphi = 0.104$), a head-rise-coefficient decrease of approximately 6 percent from the noncavitating value occurred at an H_{SV} of 15 feet representing a suction specific speed of approximately 26 500. At these latter conditions, the maximum flow is only approximately 7 percent higher than the design flow. Under these operating conditions, small excursions in flow or inlet pressure could result in significant changes in pump head rise.

Overall performance of the individual blade rows as inlet pressure is reduced may be obtained from figure 11 in which average values of cumulative head-rise coefficient across succeeding blade rows is plotted as a function of pump-inlet-flow coefficient and pump-inlet net positive suction head. At pump-inlet H_{SV} values of 136 and 38 feet, the head rise produced by the inducer and transition rotor does not drop off from the noncavitating values. However, at high flows where inducer plus transition rotor head rise is reduced (thus reducing the inlet pressure to the high-loaded stator and second-stage rotor), the performance of the stator row and second-stage rotor decrease significantly from the noncavitating level, which indicates the presence of significant amounts of cavitation. Visual studies, made under the latter operating conditions, also showed that considerable cavitation occurred in the stator and second-stage rotor but none in the inducer or transition rotors.

At a pump-inlet H_{SV} of 15 feet, the following results occurred:

(1) For flow coefficients below 0.112, cavitation occurred in the inducer only, and the decrease in overall pump head rise resulted from a decrease in inducer head rise.

(2) At flow coefficients above 0.112, cavitation occurred in all blade rows. Performance of each blade row fell off from its noncavitating level.

Visual observations confirmed the occurrence of cavitation corresponding to the blade-row-performance deterioration just noted.

Radial distributions of blade-element parameters. - The effects of cavitation on the radial distributions of blade-element flow and performance parameters of the individual blade rows are illustrated by comparing values at an average pump-inlet-flow coefficient of 0.112 and pump-inlet net positive suction heads of 246 (noncavitating) and 15 feet. This particular operating point was selected because it was the flow closest to the design value at which some cavitation was occurring in all blade rows. Caviation effects on the mass-averaged head rise across the individual blade rows and on the cumulative head rise through the pump are shown in figure 12 for these two levels of inlet pressure.

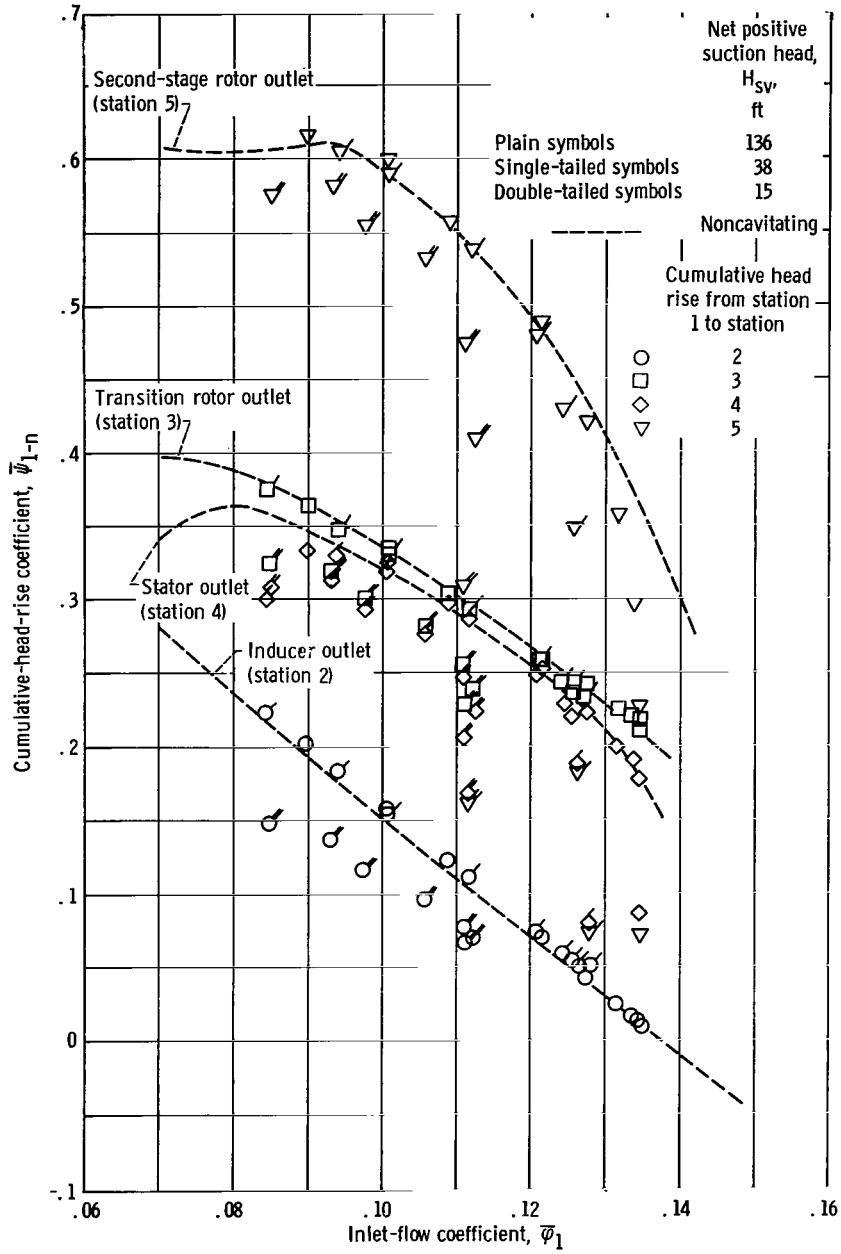

Figure 11. - Blade-row performance as pump-inlet net positive suction head is reduced.

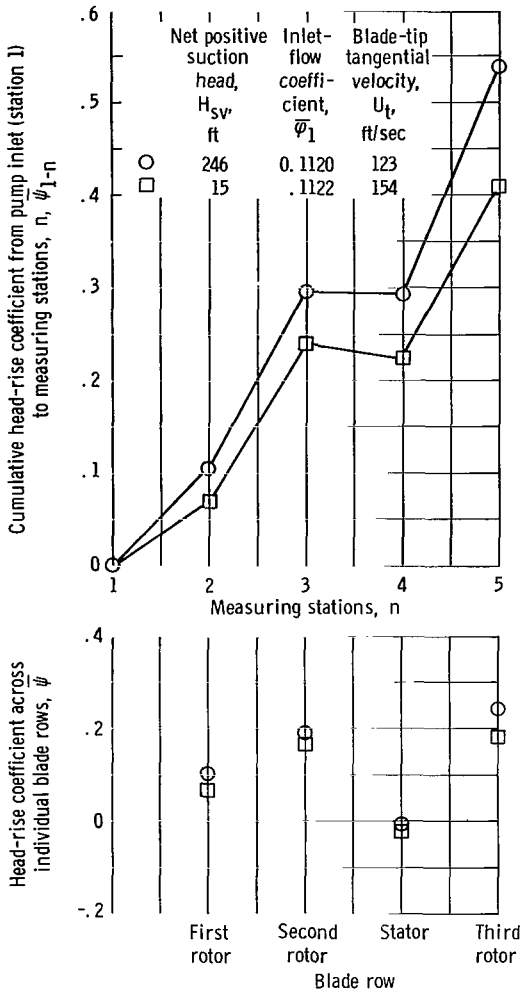

Figure 12. - Effect of cavitation on mass-averaged head rise.

The performance shown in figure 12 indicates that, at these inlet pressures and flow coefficient, some deterioration of performance because of cavitation is occurring in all blade rows.

Comparison of the radial distributions of the various blade-row flow and performance parameters is presented in figure 13 (pp. 44 to 50). Although the two operating points were obtained at different blade-tip speeds, any effect of blade speed on the parameters presented is believed to be very small, and the differences noted can be attributed to the change in inlet pressure and the resulting cavitation. When the differences of certain parameters are assessed, the relative accuracy or reliability of the data, as indicated by the checks between the integrated flow at each station and the venturi measured flow, should be recalled.

At the inducer inlet, the radial distributions of flow coefficient and incidence angle are sufficiently close that similar inlet conditions can be considered to exist. Thus, across the inducer or inducer plus transition rotor, changes in radial distribution of flow and performance parameters are caused by cavitation effects. The data indicate that, at this inlet pressure of 15 feet, cavitation affects the blade-element flow at all radii in a similar manner. While the level of performance is generally decreased, the trend with radius is maintained so that the radial distributions of flow parameters entering the downstream blade row are not significantly changed. Further examination of the data indicates that this same observation applies to data measured at all stations. It appears that the changes of blade-element parameters for all blade rows are primarily due to cavitation effects and not to significant changes in the blade-element radial matching from cavitation in upstream blade rows. It further appears that the effects of cavitation on the blade-element parameters are generally similar in all blade rows and can be discussed generally. Visual observations verify that cavitation was occurring in all blade rows at this flow coefficient and inlet pressure.

Across all rotating-blade rows, the head-rise coefficient and efficiency at the lower level of inlet pressure are decreased from the noncavitating values at all radii. One

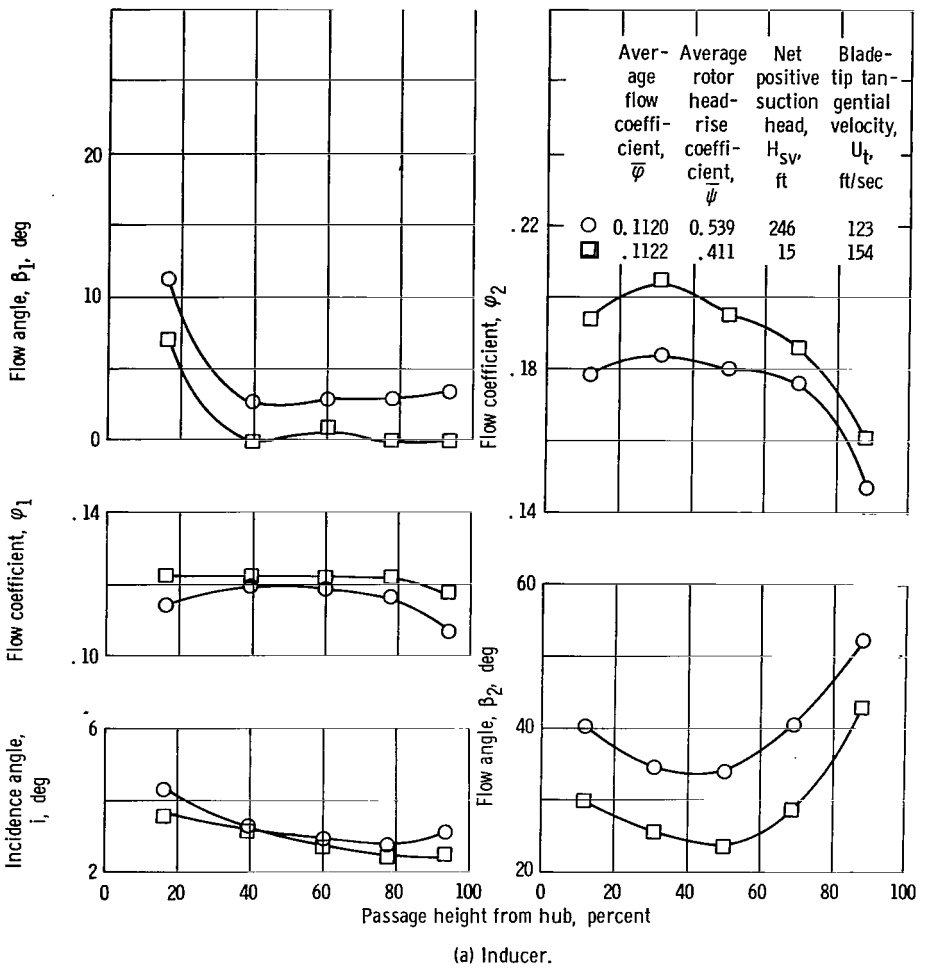

(a) Inducer.

Figure 13. - Effect of cavitation on radial distributions of blade-element parameters.

reason for this is the generally higher levels of loss coefficient during cavitating operation. A second reason is the generally lower levels of ideal head rise that accompany the occurrence of cavitation. The latter is believed to be due primarily to the lower amount of fluid turning (higher deviation angles) that can be accomplished coincident with the formation and subsequent collapse of a cavity along the blade surface.

These data indicate that, at a constant inlet-flow coefficient of 0.112, as inlet pressure was reduced until cavitation resulted in a reduction in overall head rise, cavitation produced the following results:

(1) It affected blade-element parameters at all radial locations such that radial distributions of flow entering succeeding blade rows were maintained, and significant variations of radial blade matching did not occur.

(2) It effected a decrease of head-rise coefficient and efficiency across all blade elements resulting from a general increase in the magnitude of loss coefficient and a

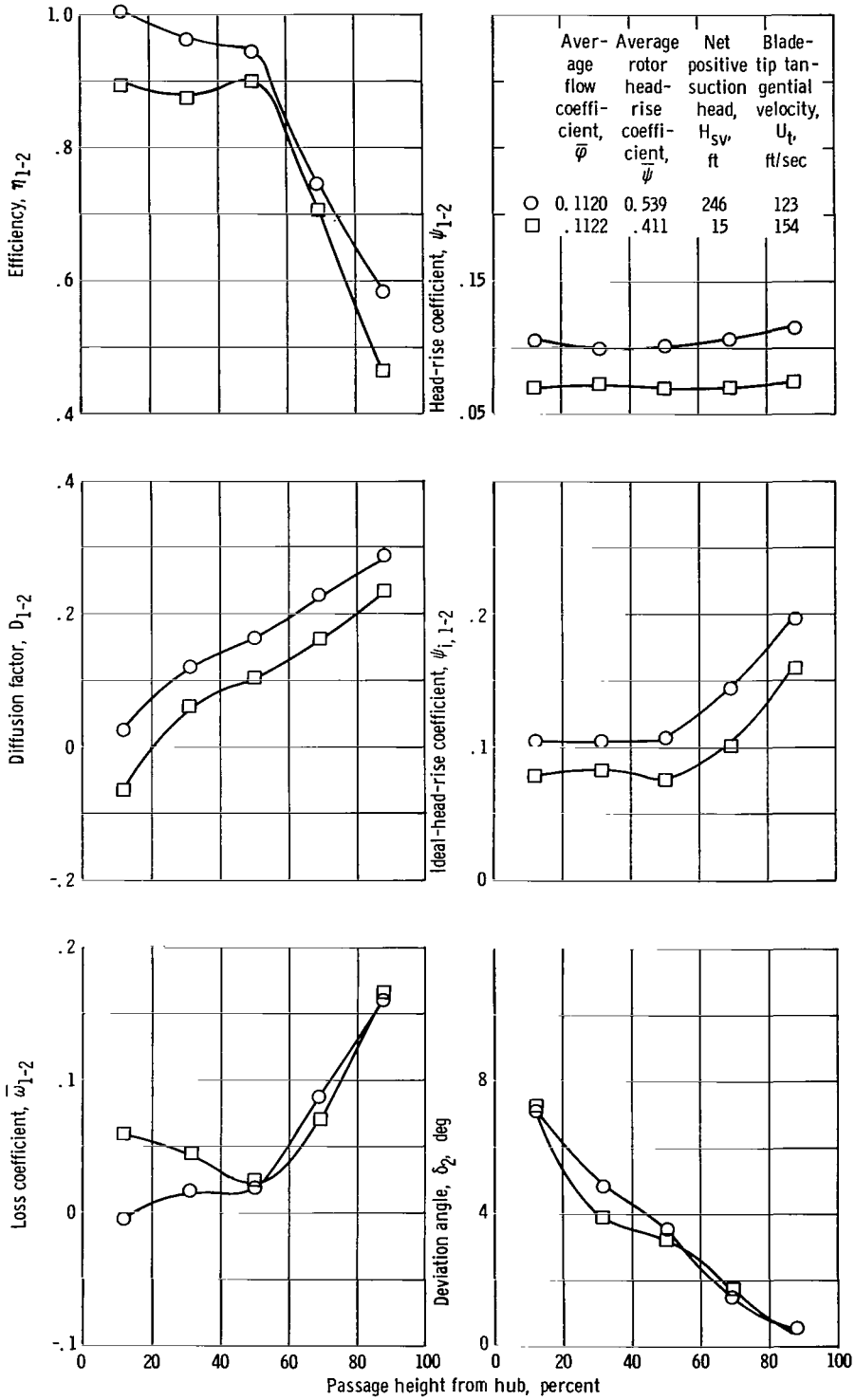

(a) Concluded.

Figure 13. - Continued.

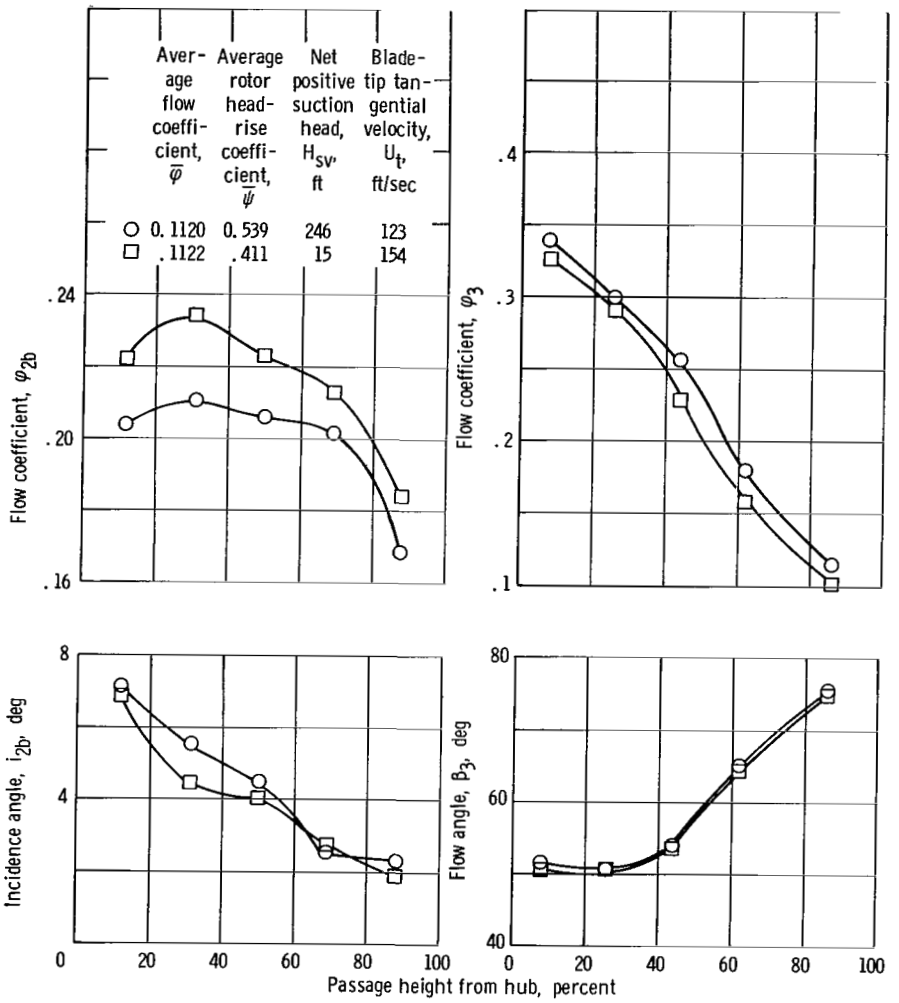

(b) Transition rotor.

Figure 13. - Continued.

decrease in energy addition.

Blade-element characteristics. - A prime objective of this investigation was to assess the use of two tandem-mounted, rotating-blade rows (inducer plus transition rotors) to obtain a high-head-rise inducer, or inlet, stage. The performance parameter levels obtained across the blade hub, mean, and tip elements of this tandem-row inducer are discussed herein. At inlet pressures from 246 (noncavitating) to 38 feet, the data defined a single curve. At an inlet pressure of 15 feet, some deviation from the noncavitating results was observed. At design flow, an inlet pressure of 15 feet represents a suction specific speed of 26 500. Blade-element characteristics for the tandem-row inducer are presented in figure 14 (pp. 51 to 53) for inlet pressures of 246 and 15 feet. For reference, the performance parameters are compared with values obtained from the flat-plate inducer of reference 4.

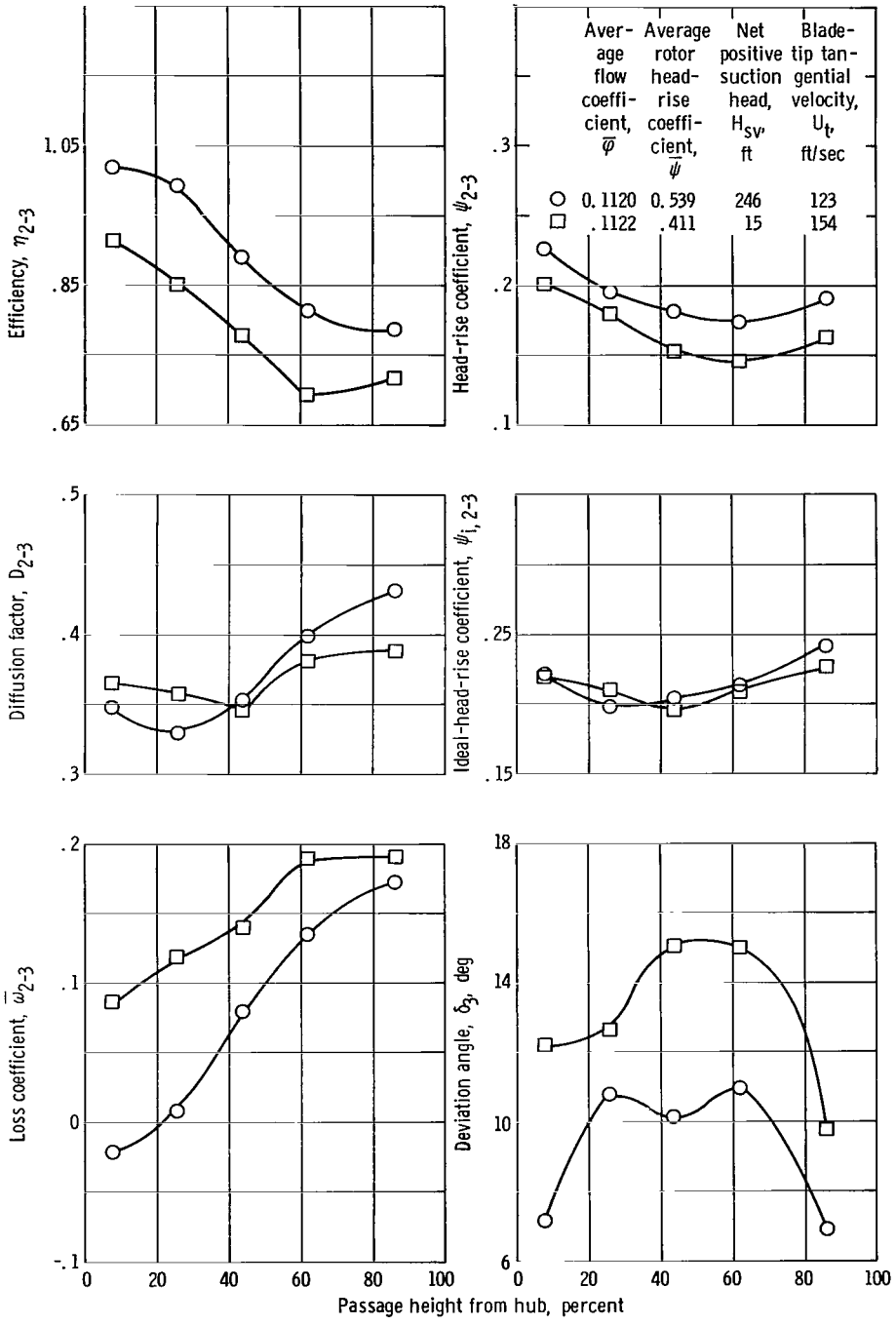

(b) Concluded.

Figure 13. - Continued.

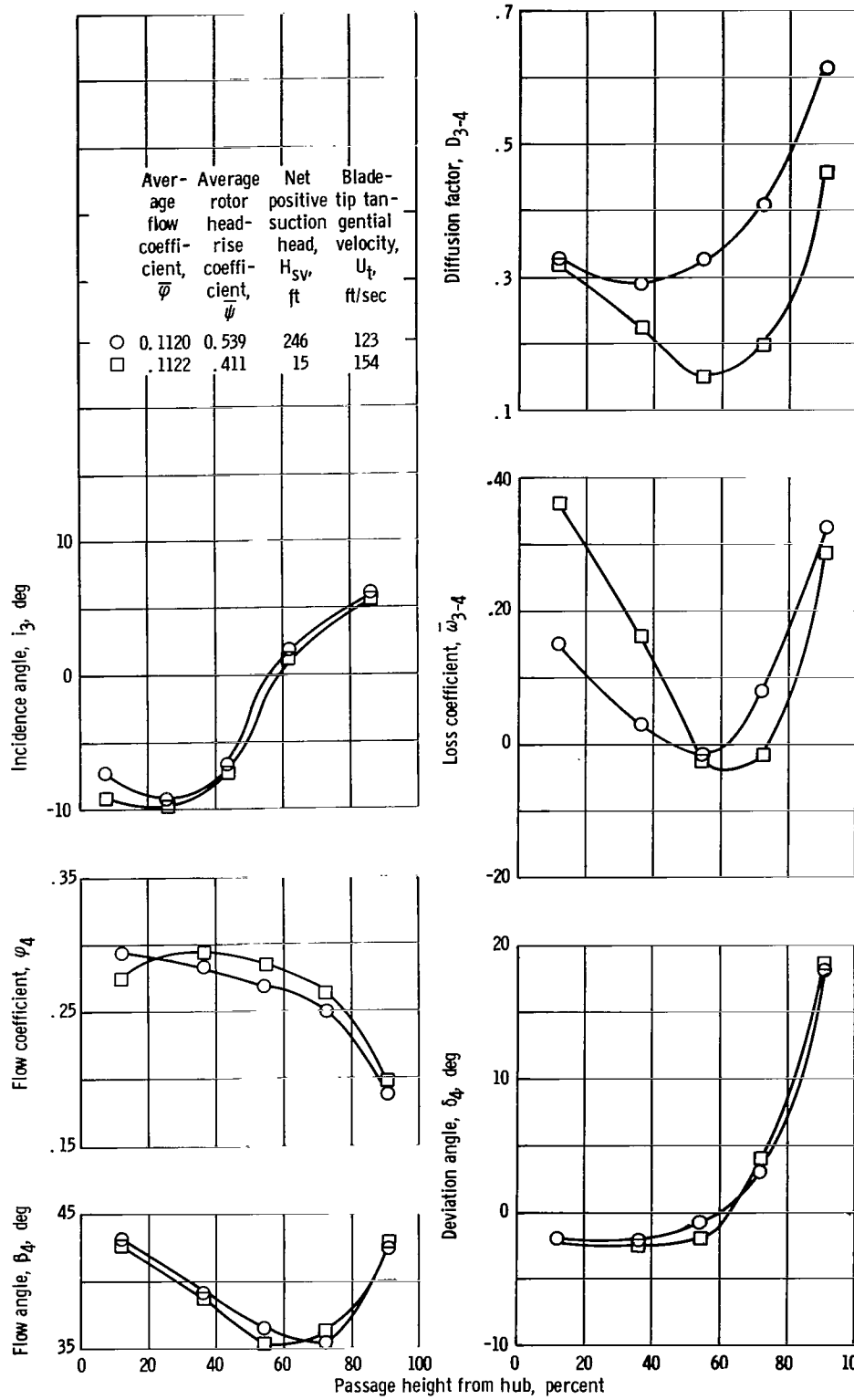

(c) Stator.

Figure 13. - Continued.

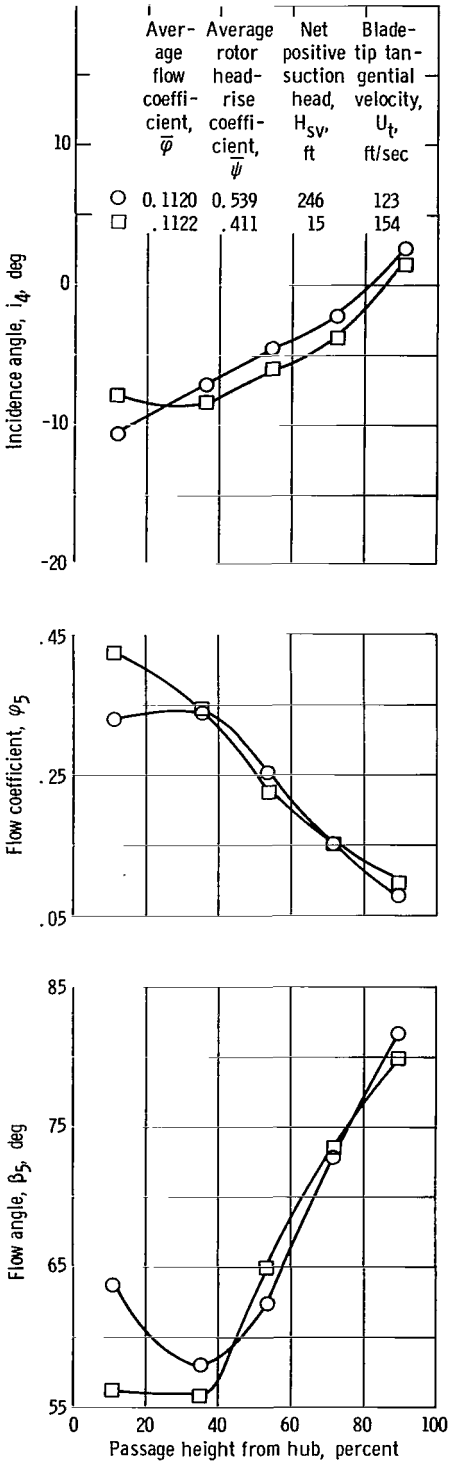

(d) Second-stage rotor.

Figure 13. - Continued.

Under noncavitating flow conditions, the radial distribution of loss coefficient is typical of that measured from most high-staggered, high-solidity inducers. The loss coefficient increases with radius, and a particularly sharp increase occurs in the tip region. The magnitude of the loss coefficients is close to, or only slightly higher than, those measured from the flat-plate inducers of reference 4, even though the energy input to the tandem-row inducer is nearly doubled. As a result, this inducer produces a significantly higher head rise at a higher efficiency level in the tip region and approximately the same high levels in the blade mean and hub regions.

Diffusion factors between 0.6 and 0.7 were observed in the blade-tip region without undue increases in the loss levels over those measured in this region for the lighter loaded, flat-plate inducer rotor of reference 4 ($D_t < 0.3$). D-factor levels at the mean and hub are generally lower because of axial velocity increases across these sections and the lower required values of energy addition due to lower levels of loss.

The radial distributions of outlet-flow coefficient and deviation angle of this complete inducer are the same as shown for the transition rotor (station 3) in figures 8 (pp. 16 to 23) and 13 (pp. 44 to 50).

At a net positive suction head of 15 feet, a decrease in head-rise coefficient from the noncavitating values occurs across all blade elements. In general, slight decreases in the energy addition ψ_i as well as increases in loss coefficient are responsible. A noticeable decrease in incidence-angle (or flow) range is evident at the lower H_{sv}.

In summary, these blade-element-performance results indicate that an inducer configuration of this type can produce a head-rise coefficient of approximately 0.325 (D_t of 0.6 to 0.7) at efficiency levels comparable to lighter loaded inducers. A head-rise decrease of approximately 10 percent (of inducer

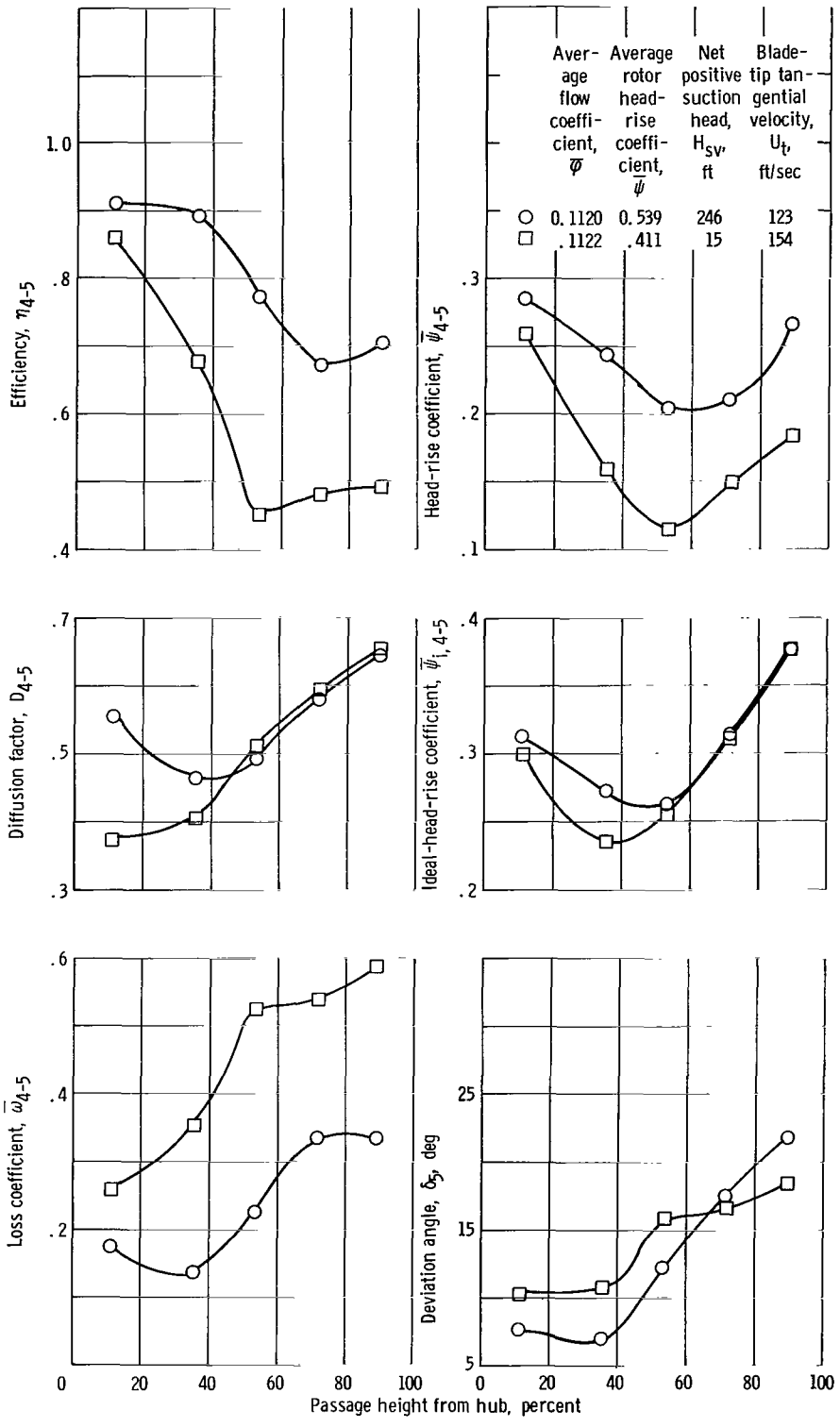

(d) Concluded.

Figure 13. - Concluded.

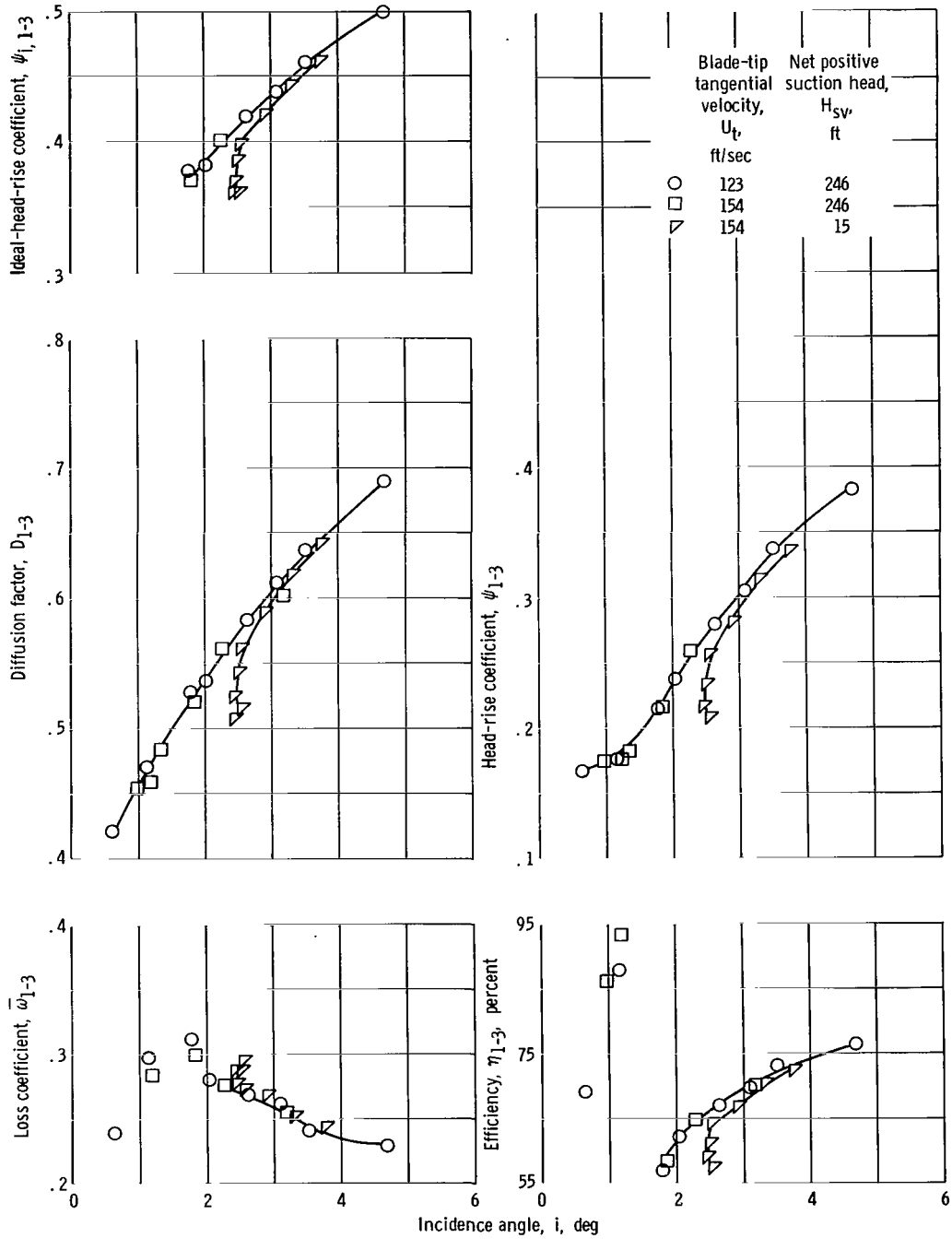

(a) Radius ratio, 0.9600 (near tip).

Figure 14. - Blade-element-performance parameters for combined inducer and transition rotors.

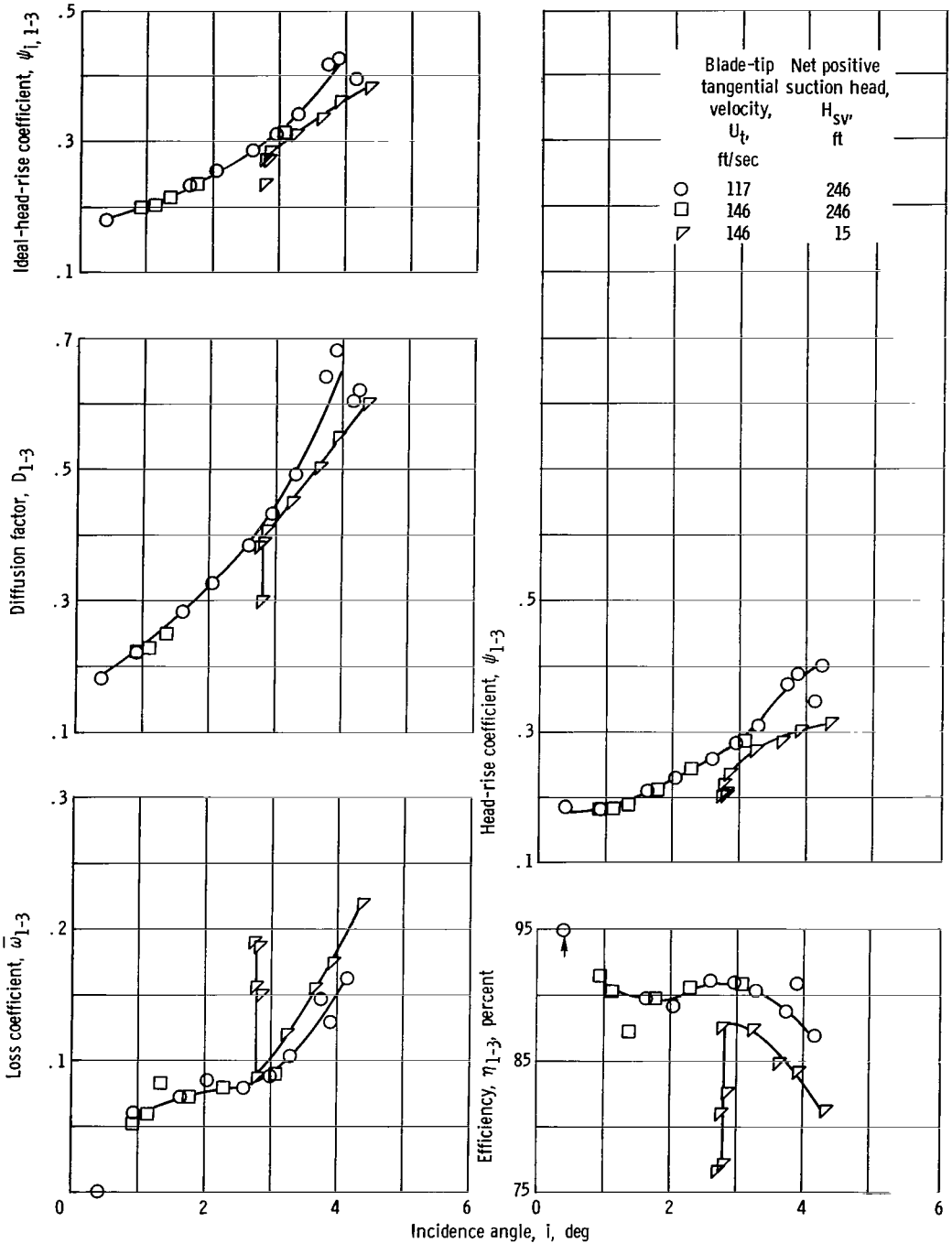

(b) Radius ratio, 0.813 (mean).

Figure 14. - Continued.

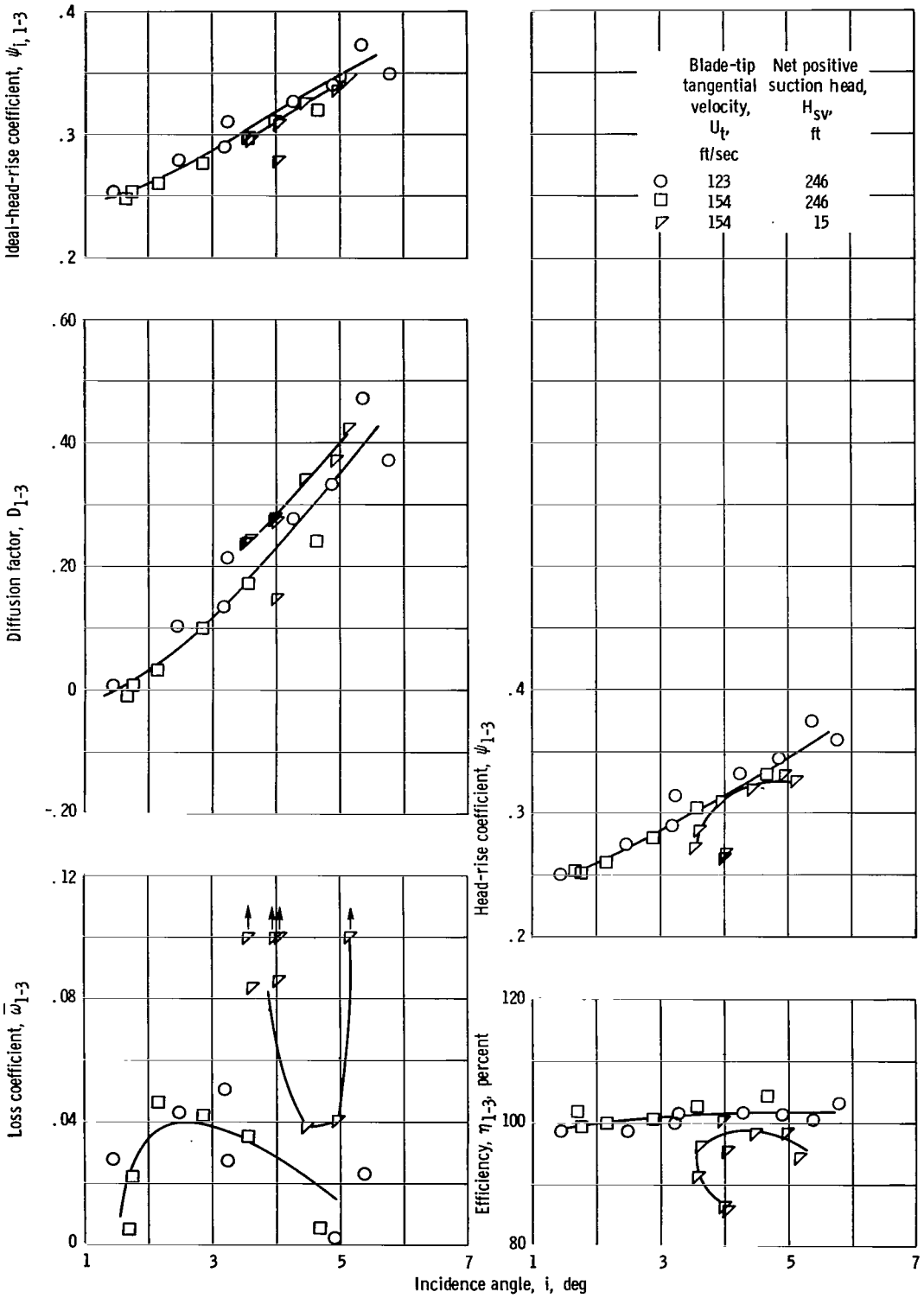

(c) Radius ratio, 0.675 (near hub).

Figure 14. - Concluded.

head rise) occurred at a suction specific speed of 26 500. The blade-element-performance results did not indicate any significant interaction effects. The two rotating-blade rows, however, were spaced a sufficient axial distance to permit traversing of the passage with the probes shown in figure 3 (p. 8). It is not evident whether or not any variations in performance would result if this axial spacing were reduced such as would apply in a normal application.

SUMMARY OF RESULTS

A two-stage, high-suction-specific-speed, axial-flow pump was tested in water. The inlet stage was composed of a 3-blade, cambered inducer rotor plus a tandem-mounted, 19-blade, transition rotor and followed by a stator-blade row. The inlet stage was succeeded by a highly loaded, second-stage rotor row. Detailed measurements of the radial distributions of flow conditions at the inlet and outlet of each blade row were made. Flow and performance parameters across a number of selected blade sections, or blade elements, were calculated. Analysis of these blade-element parameters indicated the following principal results:

1. Measured deviation angles were significantly larger than the predicted design values for the transition and the second-stage rotors, particularly in the blade-tip regions. Because of this, the design energy addition was not achieved.

2. The combined inducer and transition rotors that compose the complete rotating element of the first stage operated satisfactorily and deserve further consideration as a high-head-rise inducer configuration. At design flow, an overall head-rise coefficient of 0.325 was produced. This head-rise coefficient was nearly constant across the blade span and was obtained at efficiencies of 0.72, 0.92, and 0.99 across the tip, mean, and hub streamlines, respectively. Approximately a 10 percent decrease in head-rise coefficient occurred at a suction specific speed of 26 500. No significant blade-row-interaction effects were observed. The two rotor rows, however, operated with sufficient axial spacing to permit survey probes to be inserted. Any effect of reducing this axial clearance space on the performance results could not be evaluated.

3. When flow was reduced from design to a flow coefficient of 0.09 (86.5 percent of design flow), an eddy, or reverse-flow, region was measured in the blade-tip region at the inlet to the inducer rotor. Significant changes in the radial distribution of flow conditions occurred across the inducer and transition rotors so that the blade sections of the stators and second-stage rotor were mismatched. Losses across these two blade rows rose significantly, and the head rise produced by the second stage did not increase over its design-flow output.

4. The flow coefficient of 0.140 is the approximate high flow limit to a useful oper-

ating range for this pump. At this reduced-incidence-angle operation, the blade sections of the inducer rotor do not produce any head rise, and the reduced head rise produced by the second-stage rotor approximately compensates the increased losses across the stator row.

5. At an inlet-flow coefficient of 0.112, a comparison of radial distributions of blade-element parameters obtained at pump-inlet net positive suction heads of 246 (noncavitating) and 15 feet (pump head decrease of approximately 6 percent from noncavitating value) indicated that cavitation affected performance of all blade rows, generally resulted in higher values of deviation angle and loss coefficient, and affected parameters across all blade elements so that radial distributions were not significantly changed from noncavitating distributions.

Lewis Research Center,
National Aeronautics and Space Administration,
Cleveland, Ohio, November 2, 1966
128-31-06-28-22.

APPENDIX A

SYMBOLS

c	blade chord, in.
D	diffusion factor, eq. (B3)
g	acceleration due to gravity, 32.17 ft/sec^2
H	total head, ft
ΔH	head rise, ft
H_{sv}	net positive suction head, $H_e - h_v$, ft
h	static head, ft
h_v	vapor pressure, ft
i	incidence angle (angle between inlet-flow direction and tangent to blade mean camber line at leading edge), deg
n	measuring station
Q	flow rate, gal/min
r	radius, ft (unless otherwise indicated)
Δr	change in radius, ft (unless otherwise indicated)
t	blade thickness
U	blade tangential velocity, ft/sec
V	velocity, ft/sec
β	flow angle with respect to axial direction, deg
$\Delta\beta$	change in relative flow angle, deg
γ	blade setting angle (angle between blade chord and axial direction), deg
δ	deviation angle (angle between outlet-flow direction and tangent to blade mean line at trailing edge), deg
η	efficiency
κ	blade angle (angle between tangent to blade mean camber line and axial direction), deg
σ	blade solidity (ratio of blade chord to blade tangential spacing)
φ	flow coefficient, V_z/U_{t_e}
φ^o	blade camber angle, deg
ψ	rotor head-rise coefficient, $g\,\Delta H/(U_t)_o^2$
$\overline{\omega}$	loss coefficient, eq. (B4a)

Subscripts:

e	entrance of blade row
h	hub
i	ideal
le	blade leading edge
max	maximum
ml	minimum loss
n	axial station, see fig. 1
o	outlet of blade row
R	reference value
t	tip
te	blade trailing edge

v measured with venturi flowmeter

z axial component

θ tangential component

1 inducer-inlet measuring station

2 inducer-outlet and transition-rotor-inlet measuring station

3 transition-rotor-outlet and stator-inlet measuring station

4 stator-outlet and second-stage rotor-inlet measuring station

5 second-stage rotor-outlet measuring station

Superscripts:

$\bar{}$ averaged quantity

' relative

APPENDIX B

BLADE-ELEMENT EQUATIONS AND OVERALL PARAMETERS

Blade-Element Equations

The blade-element equations can be defined as follows:

Ideal head rise (energy input):

$$\Delta H_i = \frac{U_o V_{\theta_o} - U_e V_{\theta_e}}{g} = \Delta H + \overline{\omega} \frac{V'^2_e}{2g} \tag{B1}$$

Efficiency:

$$\eta = \frac{\Delta H}{\Delta H_i} \tag{B2}$$

Diffusion factor:

$$D = 1 - \frac{V'_o}{V'_e} + \frac{r_o V_{\theta_o} - r_e V_{\theta_e}}{2\sigma V'_e \overline{r}} = 1 - \frac{V'_o}{V'_e} + \frac{r_o V_{\theta_o} - r_e V_{\theta_e}}{(r_o + r_e)\sigma V'_e} \tag{B3}$$

When applied to the combined inducer and transition rotors (stations 1 to 3), equation (B3) was used in the form

$$D_{1\text{-}3} = 1 - \frac{V'_3}{V'_1} + \frac{1}{V'_1}\left[\frac{r_2 V_{\theta_2} - r_1 V_{\theta_1}}{\sigma_{1\text{-}2}(r_1 + r_2)} + \frac{r_3 V_{\theta_3} - r_2 V_{\theta_2}}{\sigma_{2\text{-}3}(r_2 + r_3)}\right] \tag{B3a}$$

Total-head-loss coefficient: The relative total-head-loss coefficient $\overline{\omega}$ across a blade element is defined (ref. 10) as:

$$\overline{\omega} = \frac{H'_{o_i} - H'_o}{\frac{V'^2_e}{2g}} \tag{B4a}$$

where H' is the relative total head. When applied to a rotating-blade row for incompressible flow, equation (B4a) becomes

$$\overline{\omega} = \frac{\Delta H_i - \Delta H}{\frac{V'^2_e}{2g}} \tag{B4b}$$

When applied to a stationary blade row, equation (B4a) becomes

$$\overline{\omega} = \frac{H_e - H_o}{\frac{V_e^2}{2g}} \tag{B4c}$$

Incidence angle:

$$i = \beta'_i - \kappa_{le} \tag{B5}$$

Deviation angle:

$$\delta = \beta'_o - \kappa_{te} \tag{B6}$$

Average Methods to Obtain Overall Parameters

Allowance is made for the hub and casing boundary layers in the two end terms of each of the following:

Mass-averaged head rise:

$$\overline{\Delta H} = \overline{H}_o - \overline{H}_e = \frac{\sum_{r_h}^{r_t} r_o V_{z_o} H_o \Delta r_o}{\sum_{r_h}^{r_t} r_o V_{z_o} \Delta r_o} - \frac{\sum_{r_h}^{r_t} r_e V_{z_e} H_e \Delta r_e}{\sum_{r_h}^{r_t} r_e V_{z_e} \Delta r_e} \tag{B7}$$

Mass-averaged energy addition (ideal head rise):

$$\overline{\Delta H_i} = \frac{\overline{U_o V_{\theta_o}}}{g} - \frac{\overline{U_e V_{\theta_e}}}{g} = \frac{\frac{1}{g}\sum_{r_h}^{r_t} r_o V_{z_o} U_o V_{\theta_o} \Delta r_o}{\sum_{r_h}^{r_t} r_o V_{z_o} \Delta r_o} - \frac{\frac{1}{g}\sum_{r_h}^{r_t} r_e V_{z_e} U_e V_{\theta_e} \Delta r_e}{\sum_{r_h}^{r_t} r_e V_{z_e} \Delta r_e} \tag{B8}$$

Overall efficiency:

$$\overline{\eta} = \frac{\overline{\Delta H}}{\overline{\Delta H_i}} \tag{B9}$$

Mass-averaged head-rise coefficient:

$$\overline{\psi} = \frac{g\overline{\Delta H}}{U_{t_o}^2} \tag{B10}$$

Average flow coefficient (no boundary-layer correction):

$$\overline{\varphi}_1 = \frac{Q_v}{448.8\pi(r_t^2 - r_h^2)U_{t_1}} \tag{B11}$$

REFERENCES

1. Sandercock, Donald M.; and Crouse, James E.: Design and Overall Performance of a Two-Stage Axial-Flow Pump with a Tandem-Row Inlet Stage. NASA TN D-2879, 1965.

2. Crouse, James E.; Montgomery, John C.; and Soltis, Richard F.: Investigation of the Performance of an Axial-Flow-Pump Stage Designed by the Blade-Element Theory - Design and Overall Performance. NASA TN D-591, 1961.

3. Soltis, Richard F.; Anderson, Douglas A.; and Sandercock, Donald M.: Investigation of the Performance of a 78° Flat-Plate Helical Inducer. NASA TN D-1170, 1962.

4. Sandercock, Donald M.; Soltis, Richard F.; and Anderson, Douglas A.: Cavitation and Noncavitation Performance of an 80.6° Flat-Plate Helical Inducer at Three Rotational Speeds. NASA TN D-1439, 1962.

5. Anderson, Douglas A.; Soltis, Richard F.; and Sandercock, Donald M.: Performance of 84° Flat-Plate Helical Inducer and Comparison with Performance of Similar 78° and 80.6° Inducers. NASA TN D-2553, 1964.

6. Carter, A. D. S.; and Hughes, Hazel P.: A Theoretical Investigation into the Effects of Profile Shape on the Performance of Airfoils in Cascade. Rept. No. R & M. 2384, British A.R.C., 1946.

7. Lieblein, Seymour; and Ackley, Richard H.: Secondary Flows in Annular Cascades and Effects on Flow in Inlet Guide Vanes. NACA RM E51G27, 1951.

8. Crouse, James E.; and Sandercock, Donald M.: Blade-Element Performance of 0.7 Hub-Tip Radius Ratio Axial-Flow-Pump Rotor with Tip Diffusion Factor of 0.43. NASA TN D-2481, 1964.

9. Johnsen, Irving A.; and Bullock, Robert O., eds.: Aerodynamic Design of Axial-Flow Compressors. NACA RM E56B03a, vol. II, 1956.

10. Lieblein, Seymour; Schwenk, Francis C.; and Broderick, Robert L.: Diffusion Factor for Estimating Losses and Limiting Blade Loadings in Axial-Flow-Compressor Blade Elements. NACA RM E53D01, 1953.

NASA-Langley, 1967 —— 12 E-3437

"The aeronautical and space activities of the United States shall be conducted so as to contribute . . . to the expansion of human knowledge of phenomena in the atmosphere and space. The Administration shall provide for the widest practicable and appropriate dissemination of information concerning its activities and the results thereof."

—NATIONAL AERONAUTICS AND SPACE ACT OF 1958

NASA SCIENTIFIC AND TECHNICAL PUBLICATIONS

TECHNICAL REPORTS: Scientific and technical information considered important, complete, and a lasting contribution to existing knowledge.

TECHNICAL NOTES: Information less broad in scope but nevertheless of importance as a contribution to existing knowledge.

TECHNICAL MEMORANDUMS: Information receiving limited distribution because of preliminary data, security classification, or other reasons.

CONTRACTOR REPORTS: Scientific and technical information generated under a NASA contract or grant and considered an important contribution to existing knowledge.

TECHNICAL TRANSLATIONS: Information published in a foreign language considered to merit NASA distribution in English.

SPECIAL PUBLICATIONS: Information derived from or of value to NASA activities. Publications include conference proceedings, monographs, data compilations, handbooks, sourcebooks, and special bibliographies.

TECHNOLOGY UTILIZATION PUBLICATIONS: Information on technology used by NASA that may be of particular interest in commercial and other non-aerospace applications. Publications include Tech Briefs, Technology Utilization Reports and Notes, and Technology Surveys.

Details on the availability of these publications may be obtained from:

SCIENTIFIC AND TECHNICAL INFORMATION DIVISION

NATIONAL AERONAUTICS AND SPACE ADMINISTRATION

Washington, D.C. 20546